Neutron-^{40}Ca mean field between −80 and +80 MeV from a dispersive optical-model analysis

C. H. Johnson
Oak Ridge National Laboratory, Oak Ridge, Tennessee 37831

C. Mahaux
Institut de Physique B5, Université de Liège, B-4000 Liège 1, Belgium
(Received 2 May 1988)

The n-^{40}Ca complex mean field is derived from a dispersive optical-model analysis of the available experimental cross sections. In this analysis the real part of the mean field contains dispersive contributions which are derived from the imaginary part by means of a dispersion relation. These dispersive contributions must be added to the Hartree-Fock potential which is assumed to have a Woods-Saxon shape, with a depth $V_H(E)$ that depends exponentially upon energy. The input experimental data are 14 differential cross sections in the energy domain (5.3, 40.0 MeV), five polarization cross sections in the domain (9.9, 16.9 MeV), and the total cross section in the domain (2.5, 80 MeV). The resulting optical-model potential is an analytic function of energy. It can thus be extrapolated towards negative energies, where it should be identified with the shell-model potential. This extrapolation yields good agreement with the experimental single-particle energies in the two valence shells of ^{40}Ca. The model also predicts the radial shape and the occupation probabilities of the single-particle orbits and the spectroscopic factors of the single-particle excitations. In order to reproduce the experimental energies of the deeply bound $1p$ and $1s$ orbits, one must use a linear rather than an exponential energy dependence of $V_H(E)$ at large negative E. It is shown that this is precisely the behavior expected from the fact that the energy dependence of $V_H(E)$ actually represents the nonlocality of the original microscopic Hartree-Fock field. The model also correctly predicts the distribution of the single-particle strength of the $1d\frac{5}{2}$ excitation in ^{39}Ca. The calculated distributions of the $1p$ strength in ^{39}Ca and of the $1f\frac{5}{2}$ strength in ^{41}Ca show that the available experimental information extends over less than half the expected peak, whose energy is thus poorly known experimentally. In the energy domain (2.5, 9 MeV) the predicted total cross section deviates from the experimental data; this reflects the fact that at low energy the calculated cross section is very sensitive to small modifications of the mean field.

I. INTRODUCTION

The "dispersive optical model"[1] explicitly incorporates the dispersion relation which connects the real to the imaginary part of the mean field. Its interest is manifold, in particular: It reduces the number of adjustable parameters in the optical-model analysis, since the real and imaginary parts of the optical model are inter-related; it provides an analytic way of extrapolating the real part of the mean field from positive towards negative energies, i.e., of calculating the shell-model potential from the optical-model potential; it includes effects associated with the coupling of the single-particle degree of freedom to collective excitations. This couplings gives rise to a characteristic energy dependence of the potential radius near the Fermi energy. It yields the occupation probabilities and spectroscopic factors of single-particle excitations and thus provides valuable information on the limitation of the independence particle model.

The dispersive optical-model analysis has been developed and applies to the n-^{208}Pb system in Ref. 1. The present paper is devoted to the n-^{40}Ca system. Our main motivation is fourfold. (i) In order to demonstrate the practicability of the dispersive optical-model analysis, it is necessary to investigate several systems. (ii) The comparison between the results obtained for ^{40}Ca and ^{208}Pb yields information on the dependence of the mean field upon mass number and upon neutron excess. (iii) In ^{40}Ca, experimental information is available on deeply bound single-particle states; this provides a test for the extrapolation of the mean field towards large negative energies. (iv) We show how spectral functions can be calculated from the dispersive optical model and compare them with those derived from analysis of pickup and knockout reactions.

Our presentation is the following. In Sec. II we briefly recall the basic ingredients of the dispersive optical-model analysis. In Sec. III we specify the experimental cross sections which will be used as input. Section IV is devoted to the volume (Woods-Saxon shaped) contributions to the nuclear mean field; in particular we derive the parametrization of the Hartree-Fock component of the mean field. The surface-peaked contributions to the mean field are investigated in Sec. V. The energy dependence of the radius of the real part of the mean field is investigated in Sec. VI and that of the Hartree-Fock approximation to the symmetry potential in Sec. VII. In Sec. VIII we compare the predictions of our dispersive optical-model potential with the experimental differential, polarization, and total cross sections. The

calculated binding energies of the valence single-particle states are compared with the experimental values in Sec. IX. Section X is devoted to the extrapolation of our results towards large negative energies; this will lead us to study the energy dependence of the depth of the local potential that is equivalent to a nonlocal Perey-Buck mean field.[2] Section XI contains the calculation of the effective masses at the Fermi energy of the spectroscopic factors of single-particle excitations in ^{39}Ca and ^{41}Ca and of the occupation probabilities of the single-particle orbits. In Sec. XII we show how spectral functions can be estimated from the dispersive optical model, and we compare our results with the energy distribution of the single-particle strength obtained from neutron stripping, pickup and knockout experiments. A possible refinement of the parametrization of the real and imaginary parts of the mean field at low energy is discussed in Sec. XIII. Finally, Sec. XIV contains a summary and discussion.

II. DISPERSIVE OPTICAL-MODEL ANALYSIS

Inasmuch as possible we adopt the same notation as in Ref. 1. The central part of the complex nuclear mean field is denoted by

$$\mathcal{M}(r;E)=\mathcal{V}(r;E)+i\mathcal{W}(r;E) . \tag{2.1}$$

Its real part can be written in the form

$$\mathcal{V}(r;E)=\mathcal{V}_H(r;E)+\Delta\mathcal{V}(r;E) , \tag{2.2}$$

where $\mathcal{V}_H(r;E)$ is the Hartree-Fock and $\Delta\mathcal{V}$ the dispersive contributions. The latter is connected to the imaginary potential by the dispersion relation

$$\Delta\mathcal{V}(r;E)=\frac{P}{\pi}\int_{-\infty}^{\infty}\frac{\mathcal{W}(r;E)}{E'-E}dE' . \tag{2.3}$$

Here, P denotes a principal value integral. The interest of the decomposition (2.2) is that $\Delta\mathcal{V}(r;E)$ is determined by the imaginary potential. The remaining Hartree-Fock component is unknown but is expected to have an energy-independent Woods-Saxon shape:

$$\mathcal{V}_H(r;E)=V_H(E)f(X_H) , \tag{2.4}$$

$$f(X_H)=[1+\exp(X_H)]^{-1} , \tag{2.5a}$$

$$X_H=(r-R_H)/a_H , \tag{2.5b}$$

$$R_H=r_H A^{1/3} . \tag{2.5c}$$

Throughout most of the present paper we assume that the energy dependence of the Hartree-Fock depth is exponential,

$$V_H(E)=V_H(E_F)\exp[-\alpha(E-E_F)/V_H(E_F)] ; \tag{2.6}$$

E_F is the Fermi energy that will be specified below.

In this dispersive optical model, the real part of the mean field, therefore, involves only four parameters, namely $V_H(E_F)$, α, r_H, and a_H. We emphasize that these four parameters should be sufficient to determine the energy dependence of $\mathcal{V}(r;E)$ in a wide energy domain. In the present paper we consider neutron energies which range from -80 to $+80$ MeV.

One practical difficulty in using the dispersion relation (2.3) is that it involves $\mathcal{W}(r;E)$ at negative energies, for which little empirical information is available. As in Ref. 1 we make the plausible assumption that $\mathcal{W}(r;E)$ is symmetric about the Fermi energy E_F which lies half-way between the two valence shells. The dispersion relation can then be written in the following form:

$$\Delta\mathcal{V}(r;E)=\frac{2}{\pi}(E_F-E)P\times\int_{E_F}^{\infty}\frac{W(r;E')}{(E-E_F)^2-(E'-E_F)^2}dE' . \tag{2.7}$$

Note that this dispersive contribution is skew symmetric about the Fermi energy where it vanishes,

$$\mathcal{V}(r;E_F)=\mathcal{V}_H(r;E_F) . \tag{2.8}$$

Therefore, one should require that the Hartree-Fock potential reproduces the experimental value of the Fermi energy, i.e., yields bound $1d\frac{3}{2}$ and $1f\frac{7}{2}$ single-particle states whose energies are symmetric about the Fermi energy, that we take equal to

$$E_F=-12 \text{ MeV} . \tag{2.9}$$

In practice, this requirement determines the potential depth $V_H(E_F)$ at the Fermi energy once r_H and a_H have been fixed. This reduces to three the number of parameters which appear in the real part of the mean field, namely r_H, a_H, and α.

The problem then amounts to simultaneously adjust these three parameters and the imaginary part $\mathcal{W}(r;E)$ in such a way that the experimental differential, polarization, and total cross sections are fitted by the dispersive optical-model potential defined by Eqs. (2.1)–(2.6). These experimental cross sections are specified in the next section. The reliability of the dispersive optical-model analysis is measured by the goodness of the fits to the cross sections and by its predictions concerning the weakly and deeply bound single-particle states.

III. EXPERIMENTAL CROSS SECTIONS

The open and solid dots in Fig. 1 represent the differential cross sections that will be considered in our analysis. At 5.3, 5.9, 6.5, and 7.9 MeV, these dots give the n-Ca shape elastic cross section: the compound elastic contribution as calculated by Fu[3,4] has been subtracted from the experimental cross sections measured at the University of Kentucky.[5] Note that the target was natural Ca (97% ^{40}Ca). The displayed uncertainties have been estimated by combining in quadrature the experimental error[5] with the estimated $\pm 20\%$ uncertainty associated with the evaluation of the compound elastic correction. Reference 5 also contains cross sections at 2.1 and 3.3 MeV; we do not include them in our input set because at these energies the compound elastic correction is quite larger and, moreover, the energy spread of the neutron beam was too small for averaging over resonances as would be necessary to apply the optical model.

For energies larger than 9 MeV the compound elastic

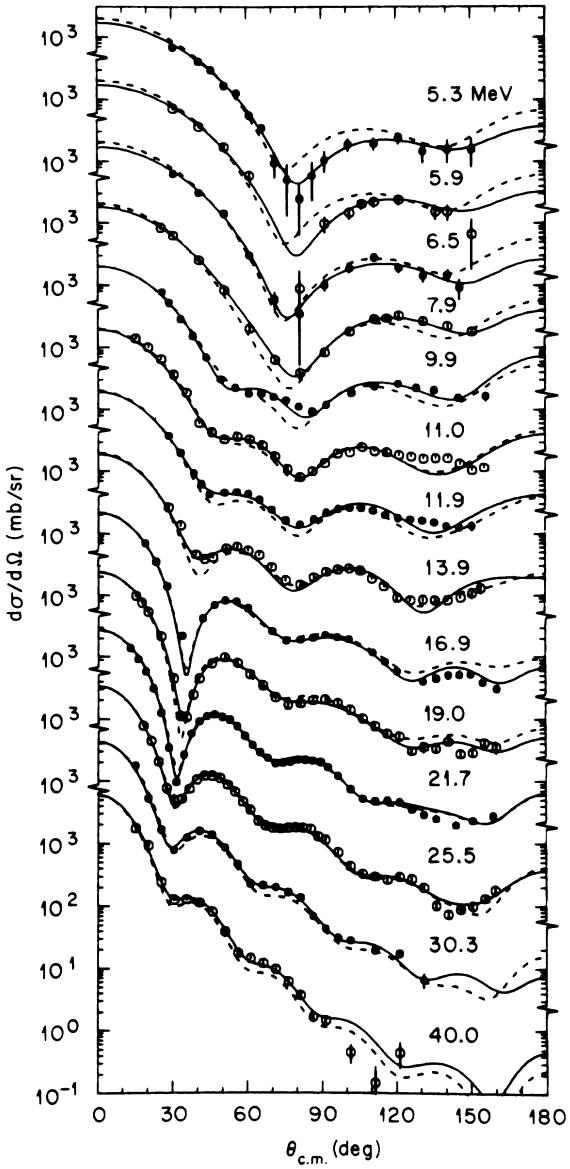

FIG. 1. Shape elastic part of the n-^{40}Ca differential cross section at 5.3, 5.9, 6.5, 7.9, 9.9, 11.0, 11.9, 13.9, 16.9, 19.0, 21.7, 25.5, 30.3, and 40.0 MeV. The dots and open circles are experimental values taken from references specified in Sec. III. The solid curves are phenomenological optical-model least-squares fits, performed at each energy independently. The dashed lines are calculated from the dispersive optical model (Sec. VIII). In each cases, the spin-orbit coupling is given by Eqs. (3.1a) and (3.1b).

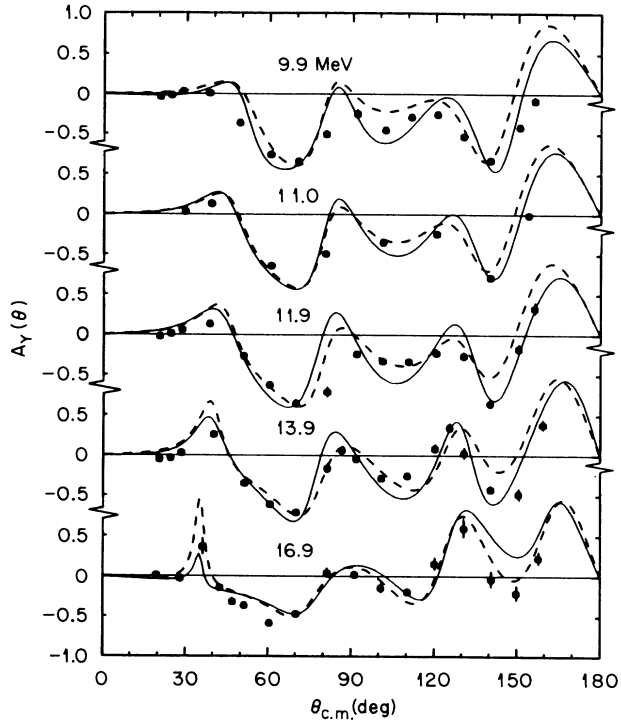

FIG. 2. Analyzing power for n-^{40}Ca scattering. The dots represent experimental values (Sec. III). The solid curves are least-squares phenomenological optical-model fits, performed independently at each energy. The dashed lines show the results of the dispersive optical-model analysis (Sec. VIII). In each case the spin-orbit coupling is given by Eqs. (3.1a) and (3.1b).

contribution can be neglected, and the symbols in Fig. 1 then represent the experimental cross sections. The data at 9.9 and 11.9 MeV (Ref. 6) and at 13.9 and 16.9 MeV (Ref. 7) have been measured at Duke University, those at 11.0 MeV (Ref. 8) and 19.0, 21.7, and 25.5 MeV (Ref. 9) at Ohio University and those at 30.3 and 40.0 MeV (Ref. 10) at Michigan State University.

Figure 2 gathers the neutron analyzing powers obtained at Duke University and reported in Refs. 7 (at 11.0, 13.9, and 16.9 MeV) and 6 (at 9.9 and 11.9 MeV).

Figure 3 shows the neutron total cross section of natural calcium, as measured at Oak Ridge National Laboratory.[11,12] Experimental values are available at more energies than shown, but we performed averages over ap-

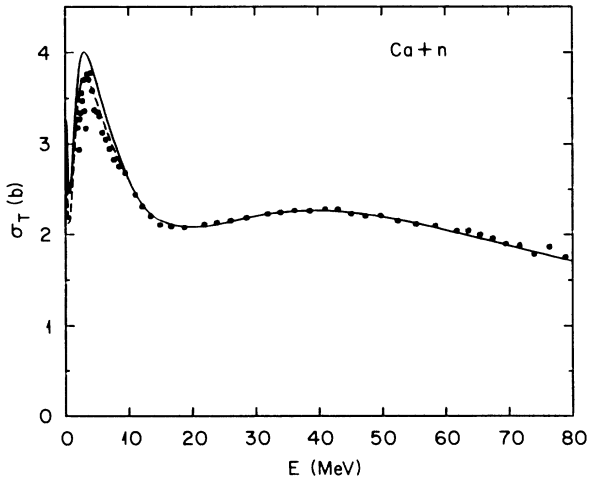

FIG. 3. Total n-Ca cross section. The dots are experimental values (Sec. III). The solid curve has been calculated from the dispersive optical-model analysis of Secs. IV–VIII and the dashed curve from the refined model of Sec. XIII.

propriate energy intervals in order to draw separate dots. These experimental data are in very good agreement with Fu's evaluation[3] of earlier measurements which extend up to 20 MeV, as well as with recent precision measurements[13] at 35, 40, 50 MeV.

In Sec. VI we shall compare these experimental data with the predictions of our dispersive optical-model analysis. In order to evaluate the quality of the agreement that will be reached, we now perform standard phenomenological optical-model fits at each energy independently. The spin-orbit coupling is taken equal to

$$\mathcal{V}_{so}(r;E)=(\sigma\cdot l)(\hbar/m_\pi c)^2 V_{so}\frac{1}{r}\frac{d}{dr}f(X_{so}) , \quad (3.1a)$$

$$V_{so}=5.40 \text{ MeV}, \quad r_{so}=1.02 \text{ fm} , \quad a_{so}=0.50 \text{ fm} . \quad (3.1b)$$

This coupling is practically identical to that determined in Ref. 7. It will be adopted throughout the present paper, and we therefore no longer explicitly refer to it.

As usual, the real part of the phenomenological optical-model potential is assumed to have a Woods-Saxon shape:

$$\mathcal{V}(r;E)=V_v(E)f(X_v) . \quad (3.2)$$

We write the imaginary part as the sum of a volume and a surface component:

$$\mathcal{W}(r;E)=\mathcal{W}_v(r;E)+\mathcal{W}_s(r;E) , \quad (3.3)$$

$$\mathcal{W}_v(r;E)=W_v(E)f(X_v) , \quad (3.4)$$

$$\mathcal{W}_s(r;E)=W_s(E)g(X_s) , \quad (3.5)$$

$$g(X_s)=-4a_s\frac{d}{dr}f(X_s) . \quad (3.6)$$

Note that here the radial shape of $\mathcal{W}_v(r;E)$ is assumed to be the same as that of $\mathcal{V}(r;E)$. This still leaves seven adjustable parameters at each energy, namely the strengths V_v, W_v, W_s and the shape parameters r_v, a_v, r_s, and a_s. As recognized by previous authors, see, e.g., Ref. 9, the experimental data are not sufficient to accurately determine all these parameters. In particular, the multiparameter least-squares searches yield volume-absorptive strengths W_v which vary from one energy to another in a somewhat erratic way about zero (positive values of W_v are frequently obtained). We therefore constrained W_v to be such that the volume integral per nucleon of $\mathcal{W}_v(r;E)$, i.e. ($A=40$),

$$J_{\mathcal{W}_v}(E)=\frac{4\pi}{A}\int_0^\infty \mathcal{W}_v(r;E)r^2dr , \quad (3.7)$$

is a smooth function of energy, namely

$$J_{\mathcal{W}_v}(E)=-B_v\frac{(E-E_F)^2}{(E-E_F)^2+\epsilon_v^2} . \quad (3.8)$$

The convenience of this parametric form has been pointed out by Brown and Rho.[14] We choose the following parameter values (see Secs. IV and V):

$$B_v=130 \text{ MeV fm}^3, \quad \epsilon_v=130 \text{ MeV} . \quad (3.9)$$

The six remaining parameters (V_v, W_s, r_v, r_s a_v, a_s) were determined by least-squares fits of the experimental cross sections associated with neutron energies larger than 8 MeV. For the smaller energies $E=5.3$, 5.9, 6.5, and 7.9 MeV the number of data points is too small to enable a reliable determination of these six parameters, and we set *a priori* $a_v=0.70$ fm. In the least-squares searches we assigned an artificially small $\pm 0.3\%$ uncertainty to the total cross section to make it play a non-negligible role in the fitting procedure. We also doubled the experimental uncertainties attached to the analyzing powers, except at 16.9 MeV, since otherwise the differential cross sections would only have played a minor role in the least-squares fits.

The results of these phenomenological optical-model fits are represented by the solid curves in Figs. 1 and 2. It is noticeable that despite the large number of adjustable parameters at each energy, the fits are not very good for scattering angles larger than 100°. This reflects the limitation of the standard optical model for light or medium-light nuclei. This limitation has also been exhibited by detailed analysis[15,16] of the scattering of protons by ^{40}Ca for which very accurate and numerous experimental cross sections are available. *A fortiori* one should not expect the dispersive optical model to yield very good fits to the experimental n-^{40}Ca cross sections. Indeed this dispersive model involves only a few parameters and aims at reproducing the cross sections at many energies, in addition to bound-state properties.

IV. VOLUME CONTRIBUTIONS TO THE MEAN FIELD

A. Fixed-geometry model

Except in Sec. XIII we henceforth use a simple "fixed-geometry model" in which we assume that the shape parameters of the Hartree-Fock and of the imaginary component of the mean field are independent of energy. More specifically, we write the imaginary part in the form (3.3), where the surface absorption is given by Eq. (3.5) while the volume absorption is now assumed to have the same Woods-Saxon shape as the Hartree-Fock contribution:

$$\mathcal{W}_v(r;E)=W_v(E)f(X_H) . \quad (4.1)$$

Equations (2.3), (3.3), (3.5), and (4.1) show that in this fixed geometry model the dispersive contribution has the following form

$$\Delta\mathcal{V}(r;E)=\Delta\mathcal{V}_v(r;E)+\Delta\mathcal{V}_s(r;E) , \quad (4.2)$$

$$\Delta\mathcal{V}_v(r;E)=\Delta V_v(E)f(X_H) , \quad (4.3)$$

$$\Delta\mathcal{V}_s(r;E)=\Delta V_s(E)g(X_s) . \quad (4.4)$$

Our motivation for adopting the same radial shape for $\mathcal{W}_v$ as for $\mathcal{V}_H$ is that the full volume component of $\mathcal{V}(r;E)$ then also has the same radial shape:

$$\mathcal{V}_v(r;E)=\mathcal{V}_H(r;E)+\Delta\mathcal{V}_v(r;E) , \quad (4.5)$$

$$\mathcal{V}_v(r;E)=V_v(E)f(X_H) , \quad (4.6)$$

$$V_v(E)=V_H(E)+\Delta V_v(E) . \quad (4.7)$$

The trends emerging from the standard optical-model fits carried out in Sec. III lead us to adopt the following numerical values:

$$r_H = 1.18 \text{ fm}, \quad a_H = 0.70 \text{ fm} , \tag{4.8}$$

$$r_s = 1.26 \text{ fm}, \quad a_s = 0.60 \text{ fm} . \tag{4.9}$$

B. Hartree-Fock parameters

The purpose of the present section is to determine the depth $V_H(E)$ of the Hartree-Fock component, i.e., the two parameters $V_H(0)$ and α, see Eq. (2.6).

We perform least-squares fits to the experimental cross sections with an optical-model potential whose imaginary part is given by Eqs. (3.3), (3.5), and (4.1), while the real part has the same form as in Eqs. (4.4)–(4.7):

$$\mathcal{V}(r;E) = V_v(E) f(X_H) + \Delta V_s(E) g(X_s) . \tag{4.10}$$

Note that the real part now explicitly includes a surface-peaked component. In these preliminary least-squares fits we adjust the parameters V_v, ΔV_s, W_v, and W_s at each energy separately. We thus require neither that they be smooth functions of energy nor, relatedly, that the dispersion relation be satisfied. We set *a priori* $W_v = 0$ for all energies smaller than 19 MeV, since the four parameter searches did not yield reliable values of W_v for these energies. Moreover, the least-squares fits yielded slightly positive values of W_v at $E = 21.7$ MeV ($W_v = 0.42$ MeV) and at $E = 30.3$ MeV ($W_v = 0.25$ MeV), in which cases we set $W_v = 0$. The least-squares adjusted values are represented by the solid dots in Fig. 4.

When the radial shape of $\mathcal{W}_v(r;E)$ is fixed according to Eqs. (4.1) and (4.8), the parametrization (3.8) and (3.9) determines a strength $W_v(E)$. This function is represented by the solid curve in Fig. 4(a). It is seen to yield a fair representation of the trend of the empirical values. This is one of our reasons for the choice of the parametrization (3.8) and (3.9) for the volume integral of $\mathcal{W}_v$, the other reason being related to the requirement that the total cross section be fitted up to 80 MeV.

Once $W_v(E)$ is fixed, the dispersion relation (2.3) determines the strength $\Delta V_v(E)$ of the dispersive contribution to the volume component of the real potential. Indeed, one has

$$\Delta V_v(E) = \frac{P}{\pi} \int_{-\infty}^{\infty} \frac{W_v(E')}{E' - E} dE' , \tag{4.11}$$

since $\mathcal{V}_v(r;E)$ and $\mathcal{W}_v(r;E)$ have been assumed to have the same radial shape.

The empirical values of the depth of the Hartree-Fock potential are then obtained from the difference

$$V_H = V_v - \Delta V_v , \tag{4.12}$$

where V_v is represented by the full dots in Fig. 4(b), while $\Delta V_v(E)$ is calculated from the dispersion relation (4.11) and is represented by the dashed curve in Fig. 4(a). These empirical values of V_H are represented by the open symbols in Fig. 4(b); the dashed curve in fig. 4(b) is a visual fit to these open symbols with the exponential law (2.6),

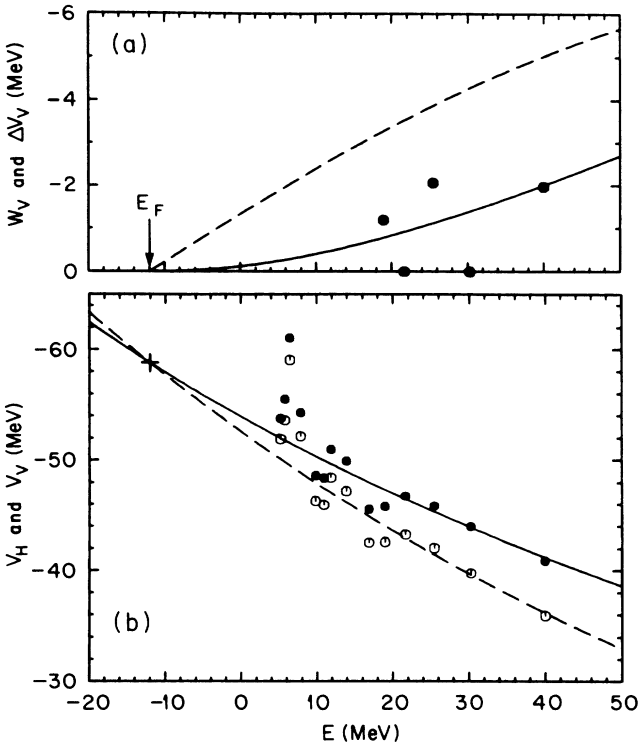

FIG. 4. The solid dots represent the values of the depth of the imaginary (top) and real (bottom) volume components of the optical-model potential obtained from the least-squares fits described in Sec. IV B. The solid curve (a) shows the Brown-Rho parametrization of $W_v(E)$ specified by Eqs. (3.8), (3.9), (4.1), and (4.8); the dashed curve (a) gives the corresponding strength $\Delta V_v(E)$ of the volume-dispersive contribution. The open symbols give the empirical value of the depth $V_H(E)$ of the Hartree-Fock potential. The dashed curve (b) is the exponential parametrization, Eqs. (2.6) and (4.13). The solid curve (b) is obtained by adding $\Delta V_v(E)$ to $V_H(E)$. The cross indicates the value of $V_H(E_F)$.

where

$$V_H(E_F) = -58.8 \text{ MeV}, \quad \alpha = -0.55 . \tag{4.13}$$

The depth at the Fermi energy has been determined by the requirement that the Hartree-Fock potential should yield $1d\frac{3}{2}$ and $1f\frac{7}{2}$ single-particle energies which are nearly symmetric about $E_F = -12$ MeV. It is seen that the exponential law (2.6) and (4.13) gives a fair representation of the average energy dependence of the empirical Hartree-Fock depth, except for the four lowest experimental energies, on which we shall return in Sec. XIII.

The solid curve in Fig. 4(b) represents the depth $V_v(E)$ obtained by summing the quantities $V_H(E)$ and $\Delta V_v(E)$ which are represented by the dashed curves in Fig. 4.

We henceforth set the central depths $V_v(E)$ and $W_v(E)$ of the real and imaginary components equal to the values represented by the solid curves in Fig. 4. Equations (4.1), (4.8), and (4.6) then fully determine the volume components $\mathcal{V}_v(r;E)$ and $\mathcal{W}_v(r;E)$ of the real and imaginary parts of the mean field. We still have to determine the

strengths $\Delta V_s(E)$ and $W_s(E)$ of the surface-peaked components. This is performed in the next section.

V. SURFACE-PEAKED CONTRIBUTIONS TO THE MEAN FIELD

In order to determine the strengths ΔV_s and W_s of the surface contributions, we perform least-squares fits of the experimental cross sections by adjusting these two parameters at each energy independently; all the other parameters are fixed as described in Sec. IV. The resulting values of W_s and ΔV_s are represented by the solid dots in Fig. 5; there, the curves are obtained from the following procedure.

We parametrize the volume integral per nucleon of the full imaginary part $\mathcal{W}=\mathcal{W}_v+\mathcal{W}_s$ by the expression

$$J_{\mathcal{W}}(E)=-B\frac{(E-E_F)^2}{(E-E_F)^2+\epsilon^2}\ , \tag{5.1}$$

where

$$B=130\ \text{MeV fm}^3,\quad \epsilon=15\ \text{MeV}\ . \tag{5.2}$$

This parametrization is suggested by the results of the standard optical-model fits performed in Sec. III and by the fit of the total cross section up to 80 MeV, see below. Equations (3.8), (3.9), (5.1), and (5.2) then determine the volume integral of the surface-peaked absorptive potential. These integrals of the imaginary components of the potential are plotted in part of Fig. 6(a); 6(b) gives the volume integrals of the corresponding dispersive corrections.

Since the geometrical shape of $\mathcal{W}_s(r;E)$ is fixed according to Eqs. (4.4) and (4.9), there exists a one-to-one correspondence between the value of the volume integral $J_{\mathcal{W}_s}$ and that of the strength $W_s(E)$, and correspondingly for $J_{\Delta\mathcal{V}_s}(E)$ and $\Delta V_s(E)$. The curves in Fig. 5 represent the quantities $W_s(E)$ and $\Delta V_s(E)$ associated with the volume integrals shown in Fig. 6. It is seen that these curves fairly well reproduce the overall trend of the empirical dots. The agreement between the solid curve and the empirical values of W_s mainly reflects the fact that the parametrization (3.8), (3.9), (5.1), and (5.2) yield a good representation of the energy dependence of the imaginary part of the optical-model potential.

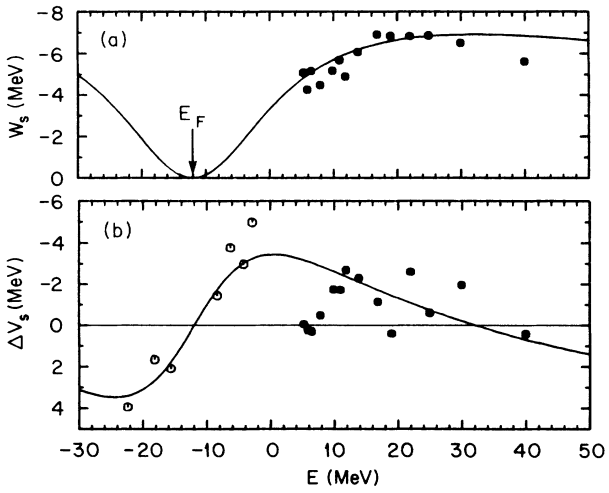

FIG. 5. The solid dots represent the empirical values of W_s (top) and ΔV_s (bottom) obtained from the two-parameter least-squares fits described in Sec. V. The solid curves correspond to the volume integrals shown in Fig. 6. The open symbols give the value of the strength $\Delta V_s(E_{nlj})$ of the surface-peaked potential which is required to reproduce the experimental value E_{nlj} of the single-particle energy, for the $1d\frac{5}{2}$, $2s\frac{1}{2}$, $1d\frac{3}{2}$, $1f\frac{7}{2}$, $2p\frac{3}{2}$, $1f\frac{5}{2}$, and $2p\frac{1}{2}$ levels.

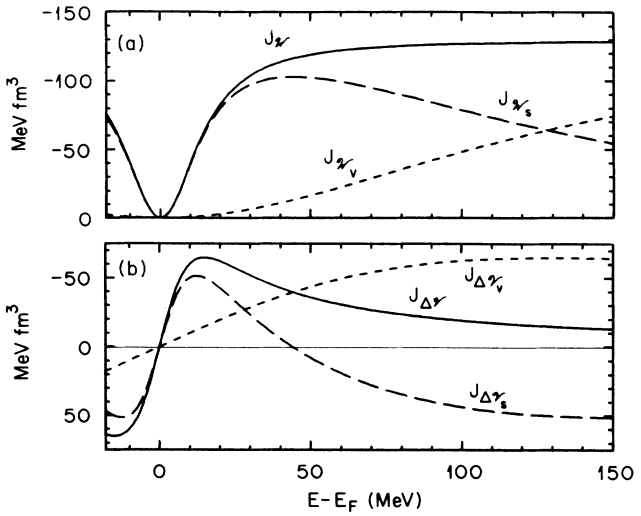

FIG. 6. (a) The energy dependence of the volume integrals per nucleon of the full ($\mathcal{W}$, solid curve), volume ($\mathcal{W}_v$, short-dashed line), and surface-peaked $\mathcal{W}_s$, long-dashed line) components of the absorptive potential, as determined by Eqs. (3.8), (3.9), (5.1), and (5.2). (b) The volume integrals per nucleon of the corresponding full, volume, and surface-peaked dispersive corrections, as calculated from the dispersion relation (2.7).

The agreement between the predicted solid curve for $\Delta V_s(E)$ and the empirical solid dots is only qualitative. Several comments are in order. (i) The agreement between the predicted solid curve for $\Delta V_s(E)$ and the empirical values becomes much more striking when this comparison is extended to negative energies, as we now describe. The open symbols in Fig. 5 are located at the experimental single-particle energies E_{nlj} (these will be specified in Sec. IX) and have been obtained in the following way. We consider the potential

$$\mathcal{V}(r;E_{nlj})=V_v(E_{nlj})f(X_H)+\Delta V_s(E_{nlj})g(X_s)\ , \tag{5.3}$$

in which $V_v(E_{nlj})$ is determined by the solid curve in Fig. 4(b), while the shape parameters are given by Eqs. (4.8) and (4.9). The open symbols in Fig. 5 represent the strength $\Delta V_s(E_{nlj})$ for which the single-particle energy calculated from $\mathcal{V}(r;E_{nlj})$ coincides with the experimental value E_{nlj}. It is seen that the curve for $\Delta V_s(E)$ reproduces the trend of the empirical open and solid dots. (ii) The solid dots located at the lowest scattering energies

(5.3, 5.9, 6.5, and 7.9 MeV) deviate from the solid curve for $\Delta V_s(E)$. We recall that the empirical potential central depths associated with these energies already had a peculiar behavior in Fig. 4(b); we return to this low-energy domain in Sec. XIII. (iii) The calculated $\Delta V_s(E)$ changes sign at 32 MeV. In that vicinity the radius parameter of the calculated full potential $\mathcal{V}(r;E)$ therefore becomes equal to that of its Hartree-Fock component, namely $r_H = 1.18$ fm. Actually this property is at the origin of our choice of this numerical value for r_H. Indeed, the energy domain in which $\Delta V_s(E)$ changes sign is not very sensitive to the specific parametrization of $W_s(E)$; the phenomenological optical-model fits (performed in Sec. III or in Ref. 9) to the experimental cross sections indicate that r_V is close to 1.18–1.20 fm for E close to 30 MeV.

VI. ENERGY DEPENDENCE OF THE REAL POTENTIAL

Equation (4.2) expresses the dispersive contribution $\Delta\mathcal{V}$ as the sum of a Woods-Saxon shape component $\Delta\mathcal{V}_v$ and a surface-peaked component $\Delta\mathcal{V}_s$. These three quantities are represented in Fig. 7. The behavior of $\Delta\mathcal{V}_v(r;E)$ and of $\Delta\mathcal{V}_s(r;E)$ can be understood from their volume integral shown in Fig. 6(b). As the neutron energy increases from zero to 100 MeV the depth of the volume contribution increases; the surface-peaked contribution is attractive for $E < 32$ MeV and then becomes repulsive.

Since the radial shape of the dispersive contribution depends upon energy, the radial shape of the full potential $\mathcal{V}(r;E)$ is also energy dependent, although that of its Hartree-Fock component $\mathcal{V}_H(r;E)$ is constant. In order to evaluate the energy dependence of the potential radius we proceed as follows. We first calculate the volume integral per nucleon $J_{\mathcal{V}}(E)$ of $\mathcal{V}(r;E)$; this quantity is represented by the solid curve in Fig. 8. We then assume that $\mathcal{V}(r;E)$ has a Woods-Saxon shape, Eq. (3.2), with a depth $V_v(E)$ given by the solid curve in Fig. 4(b) and with a diffuseness equal to

$$a_v = a_H = 0.70 \text{ fm} . \tag{6.1}$$

We checked that these assumptions are quite accurate. From the values of $J_{\mathcal{V}}(E)$, $V_v(E)$, and a_v, one can then calculate the energy dependence of the radius parameter r_v. The result is represented by the solid curve in Fig. 9, in which the crosses and dots are empirical values. The crosses are obtained from least-squares fits which involve five adjustable parameters, namely V_v, r_v, W_s, r_s, and a_s [see Eqs. (3.2)–(3.9)], while the dots result from searches which only involve the same two adjustable parameters as the solid dots in Fig. 5(b), namely W_s and ΔV_s. Note that at the four lowest scattering energies (5.3, 5.9, 6.5, 7.9 MeV) the solid dots in Fig. 9 fall considerably below the crosses. This mainly reflects the fact that at low energy the shape parameters r_s, a_s of the surface-peaked absorption display some energy dependence: The phenomenological fits performed in Sec. III indeed indicate that at low energy these parameters average about $r_s \approx 1.37$ fm, $a_s \approx 0.30$ fm in contrast to the approximation made in

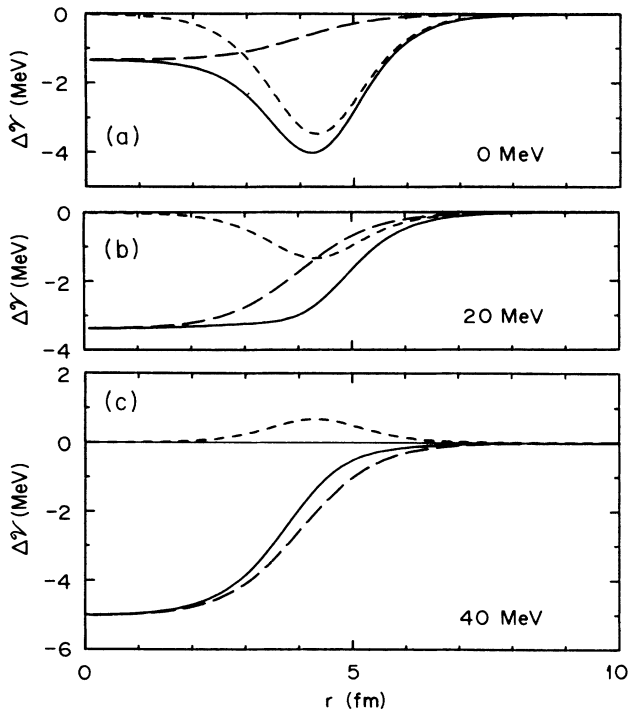

FIG. 7. (a), (b), and (c) the radial dependence of the dispersive contribution for neutron energies equal to 0, 20, and 40 MeV, respectively. In each case, the long-dashed line represents the Woods-Saxon shape component $\Delta\mathcal{V}_v$, the short-dashed line the surface-peaked component $\Delta\mathcal{V}_s$, and the solid curve their sum $\Delta\mathcal{V}$.

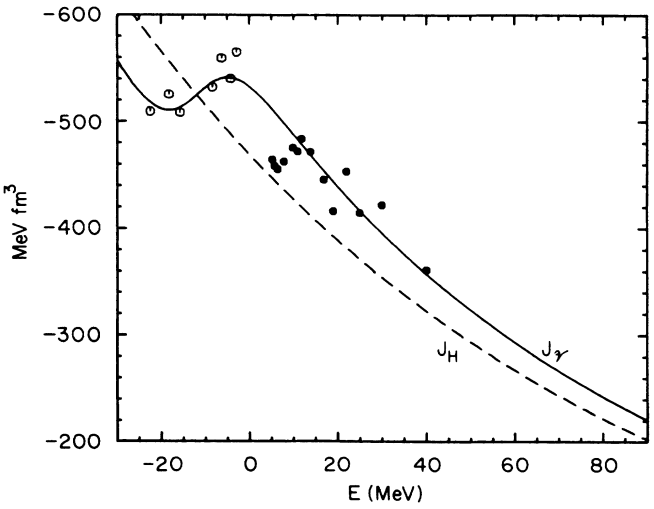

FIG. 8. Energy dependence of the volume integral per nucleon of the real potential (solid curve) and of its Hartree-Fock component (dashed line). The dots represent empirical values obtained by summing the volume and surface terms which correspond, respectively, to the solid curve in Fig. 4(b) and to the dots in Fig. 5(b).

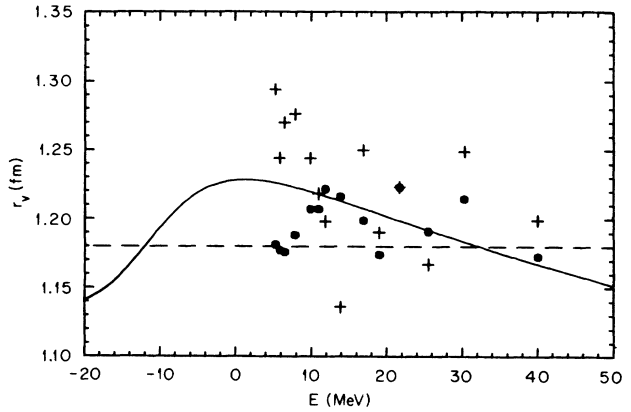

FIG. 9. Energy dependence of the radius parameter of the real potential well. The dashed horizontal line corresponds to the radius parameter $r_H = 1.18$ fm of the Hartree-Fock potential. The solid curve and the dots represent the predicted and empirical radius parameter of a Wood-Saxon potential with a diffuseness $a_v = 0.70$ fm, a depth given by the solid curve in Fig. 4(b), and a volume integral represented by, respectively, the solid curve and the dots in Fig. 8. The crosses are empirical values obtained from phenomenological optical-model analyses similar to those described in Sec. III, except that the diffuseness a_v of the real and imaginary Woods-Saxon shaped contributions was set equal to 0.70 fm.

Eq. (4.9). We return to this point in Sec. XIII.

In conclusion the radius parameter r_v obtained from the five-parameter phenomenological optical-model fits suggest that the potential radius decreases with increasing energy in the domain $E > 5$ MeV. A similar decrease had been pointed out in the case of the scattering of neutrons by ^{208}Pb.[17,18] In that as well as in the present case this decrease is in keeping with the energy dependence of the surface-peaked dispersive contribution.[1] Physically, it arises from the decreasing importance of the coupling of the incoming nucleon-to-surface excitations of the target.

VII. COMPARISON BETWEEN THE n-^{40}Ca AND THE n-^{208}Pb MEAN FIELDS

The main purpose of the present section is to compare the present n-^{40}Ca mean field, $\mathcal{V}_{Ca}(r;E)$, with the n-^{208}Pb mean field, $\mathcal{V}_{Pb}(r;E)$, which has been constructed in Ref. 1.

The dispersive contribution to the mean field is due to the coupling of the neutron to the excited states of the core. This coupling is expected to vary from one nucleus to the other in a way which is influenced by nuclear dynamics and cannot be expressed as a simple function of mass number or neutron excess. This is why here we shall only consider the Hartree-Fock component of the mean field. We recall that by definition this component is not much influenced by the coupling of the neutron to low-lying core excitations. Accordingly, it is expected to vary smoothly with mass number and neutron excess and could possibly be estimated in the framework of nuclear-matter calculations.

We first notice that the radius parameter of the neutron Hartree-Fock potential is smaller in ^{40}Ca ($r_H = 1.18$ fm) than in ^{208}Pb ($r_H = 1.24$ fm, see Ref. 1). This difference mainly reflects the dependence of the density radius upon mass number. Indeed, for $A \gtrsim 40$ the density distribution $\rho(r)$ approximately has a Woods-Saxon shape with the following radius parameter:[19]

$$r_\rho \approx 0.97 + 0.0206 A^{1/3} \text{ fm} . \tag{7.1}$$

This yields $r_\rho = 1.05$ fm for ^{40}Ca and $r_\rho = 1.10$ fm for $A = 208$. Hence the radius parameter associated with the nuclear density increases by approximately 0.05 fm when A increases from 40 to 208. This is in keeping with the 0.06-fm increase of r_H found in our analysis.

We now turn to the difference between the depths of the Hartree-Fock potentials for neutrons in ^{40}Ca and ^{208}Pb. The main origin of this difference is twofold, namely (i) the symmetry potential causes the absolute value of the depth to decrease with increasing neutron excess; (ii) the central density ρ_0 tends to decrease with increasing A. Because of the density dependence of the nucleon-nucleon effective interaction this may lead to a decrease of the potential depth with increasing mass number. Since on the average neutron excess increases with mass number the effects (i) and (ii) both tend to decrease the depth when A increases. Here we shall neglect effect (ii) because it is expected to be small for mass numbers $A > 40$. However, one should keep in mind that this neglect implies that the depth of the Hartree-Fock symmetry potential that we shall calculate is likely to be overestimated.

We denote by η the asymmetry coefficient in ^{208}Pb:

$$\eta = \frac{N-Z}{A} = 0.21 . \tag{7.2}$$

In the local-momentum approximation, the depth of the symmetry potential is given by the following expression:[20]

$$\eta V_1^H(E) = V_H^{Pb}[E + \tfrac{1}{2}\eta V_1^H(E)] - V_H^{Ca}[E - \tfrac{1}{2}\eta V_1^H(E)] . \tag{7.3}$$

The energy shifts which appear on the right-hand side of Eq. (7.3) essentially take into account the difference between the Fermi energies in ^{40}Ca and in ^{208}Pb, respectively. Accordingly, it is convenient to measure the energies from the Fermi energy[21] and to replace Eqs. (7.3) by the following prescription:

$$\eta U_1^H(E - E_F) = U_H^{Pb}(E - E_F) - U_H^{Ca}(E - E_F) , \tag{7.4}$$

where

$$U_H^{Ca}(E - E_F) = V_H^{Ca}(E - E_F^{Ca}) , \tag{7.5a}$$

$$U_H^{Pb}(E - E_F) = V_H^{Pb}(E - E_F^{Pb}) . \tag{7.5b}$$

Equations (2.6) and (4.13) yield (all energies in MeV)

$$U_H^{Ca}(E - E_F) = -58.8 \exp[-0.55(E - E_F)/58.8] , \tag{7.6a}$$

while Eq. (3.5a) of Ref. 1 gives

$$U_H^{\rm Pb}(E-E_F)=-46.4\exp[-0.31(E-E_F)/46.4]\ . \tag{7.6b}$$

Figure 10(a) shows the Hartree-Fock approximation to the depth of the symmetry potential as obtained from Eqs. (7.4)–(7.6b). These values are in semiquantitative agreement with those recently derived[20] from a comparison between the Hartree-Fock contributions to the n-^{208}Pb and p-^{208}Pb mean fields; a comparison with phenomenological values can be found in Ref. 20. We recall that the result shown in Fig. 10(a) is likely to be an overestimate because the central density is probably somewhat larger in ^{40}Ca than in ^{208}Pb. Furthermore our estimate is somewhat sensitive to the shape parameters of the Hartree-Fock potential. For instance, if the adopted value of a_H in ^{208}Pb is increased from 0.68 to 0.70 fm, the radius parameter r_H decreases from 1.24 to 1.225 fm and the calculated U_1^H decreases by about 10%.

In view of this sensitivity of the calculated symmetry potential depth upon the geometrical shape parameters one might consider the volume integral per nucleon of the symmetry potential as approximated by [see Eq. (7.4)]

$$J_1^H(E-E_F)=J_H^{\rm Pb}(E-E_F)-J_H^{\rm Ca}(E-E_F)\ . \tag{7.7}$$

This quantity is plotted in Fig. 10(b). It is also probably an overestimate. The amount of overestimate is likely to be larger than in the case of the depth of the symmetry potential because, even in the absence of any isovector component in the mean field, its volume integral per nucleon decreases with increasing mass number A since the radius parameter decreases with A.[22]

The depth show in Fig. 10(a) is thus likely to be more meaningful than the volume integral per nucleon plotted in Fig. 10(b). In both cases, however, the results should be considered as crude estimates. We emphasize that the difficulties alluded to above also mar any phenomenological use of the symmetry potential to evaluate the variation of the mean field with mass number and neutron excess.[23] In turn these difficulties are also present when one tries to define theoretically a symmetry potential by considering the modification of the microscopic mean field with the number of neutrons and protons in the target.

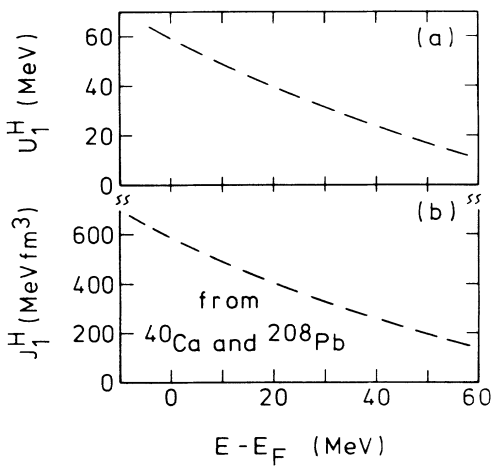

FIG. 10. Central depth (top) and volume integral per nucleon (bottom) of the symmetry potential in the Hartree-Fock approximation, as calculated from Eqs. (4.8), (7.4), (7.6a), and (7.6b).

VIII. COMPARISON WITH THE EXPERIMENTAL CROSS SECTIONS

In the present section we compare the cross sections predicted by our dispersive optical-model potential with the experimental cross sections. The imaginary part of the potentials is specified by the shape parameters of Eqs. (4.8) and (4.9) and by the strengths represented by the solid curves in Figs. 4(a) and 5(a). The real part of the potential is given by the shape parameters of Eqs. (4.8) and (4.9) and by the strengths shown by the solid curves in Figs. 4(b) and 5(b).

The predicted shape elastic differential cross sections are represented by the dashed curves in Fig. 1. The overall agreement between the calculated and experimental differential cross sections is similar to that obtained from phenomenological optical-model potentials which depend smoothly upon energy.[6,24] However, this agreement is more meaningful in the present case, for the following two main reasons. (i) Our analysis involves fewer parameters than the phenomenological ones. Indeed, the dispersive contribution to the real part of the potential is entirely determined by the imaginary part. The adjustable parameters in the real part of the potential are essentially $V_H(E_F)$, r_H, and α (Sec. IV). Among these, r_H is determined by the radius of the phenomenological real potential near 30 MeV (Sec. V). The depth $V_H(E_F)$ is determined by the requirement that the Fermi energy be reproduced, and α by the depth of the phenomenological real part near 30 MeV. Therefore very little flexibility exists for the real potential once the imaginary potential is fixed. (ii) One essential difference between the present dispersive optical-model analysis and phenomenological optical-model fits is that here the real part is required to reproduce the Fermi energy when extrapolated towards negative energies. This requirement renders the extracted potential much more meaningful from the physical point of view; it also drastically reduces the freedom when searching for optimal fits to the experimental cross sections. For instance, the Hartree-Fock potential of Ref. 25 was adjusted to the scattering cross sections only and yields −7.3 MeV for the Fermi energy instead of −12 MeV which is the experimental value.

The predicted analyzing powers are represented by the dashed curves in Fig. 2. Their agreement with the experimental values is quite good at all energies. This is particularly remarkable. Indeed, phenomenological fits with a smoothly energy-dependent optical-model potential do not yield good fits to the analyzing powers unless one "includes some physically unrealistic parameters for the spin-orbit potential."[24] More specifically, good phenomenological fits require the introduction of an imaginary part in the spin-orbit potential, and the sign of this imaginary part is at variance with theoretical expectations as

well as with empirical evidence from p-^{40}Ca analyzing powers at higher energies.[7] Here we have obtained good fits to the analyzing powers with a purely real spin-orbit coupling, Eqs. (3.1a) and (3.1b). This success is due to the existence of a surface-peaked component in the dispersive contribution to the real potential.[25]

The predicted total cross section is represented by the solid curve in Fig. 3. Its agreement with the experimental values is very good in the energy domain $10 < E < 80$ MeV. However, the model overestimates by about 5% the total cross section in the domain $2 < E < 9$ MeV. This disagreement is not unexpected. Indeed it should be kept in mind that at low energy the total cross section is dominated by very few partial waves, in the present case by the orbital angular momenta $l = 1$ and 2; this is exhibited in Fig. 11. In our dispersive optical-model analysis it is assumed that the imaginary part of the mean field is independent of the orbital angular momentum. This is an approximation. Our parametrization of $\mathcal{W}(r;E)$ might be good on the average but somewhat inaccurate for $l = 1$ or $l = 2$. Hence, it is not surprising that the total cross section at low energy is not accurately predicted by our analysis because the latter implicitly involves an average over partial waves. This average description may be somewhat inaccurate for observables that are particularly sensitive to very few partial waves. Another possible interpretation of the deviation of the predicted from the experimental total cross section below 9 MeV is that the shape parameters (4.9) of the surface-peaked absorption $\mathcal{W}_s(r;E)$ may become inappropriate at low energy; this will be considered in Sec. XIII.

IX. ENERGIES OF THE VALENCE SINGLE-PARTICLE STATES

One of the main interests of the dispersive optical-model analysis is to enable the extrapolation of the real part of the mean field from positive towards negative energies. In other words it provides a way of constructing the shell-model potential from the analytic continuation of the optical-model potential. The present section is devoted to the comparison between the predicted and experimental energies of the valence single-particle states, i.e., of the levels which belong to the ($2s$-$1d$) and ($2p$-$1f$) valence shells.

The $1f_{\frac{7}{2}}$, $2p_{\frac{3}{2}}$, $2p_{\frac{1}{2}}$, and $1f_{\frac{5}{2}}$ single-particle energies $E_{nlj} > E_F$ have been measured by means of the ^{40}Ca$(d,p)^{41}$Ca stripping reaction.[26] The $1d_{\frac{5}{2}}$, $2s_{\frac{1}{2}}$, and $1d_{\frac{3}{2}}$ single-particle energies $E_{nlj} < E_F$ have been obtained from the ^{40}Ca$(d,t)^{39}$Ca pickup reaction.[27] These experimental values are plotted in the column labeled Expt. in Fig. 12, in which the other columns contain energies calculated in, respectively, the Hartree-Fock potential $\mathcal{V}_H(r;E)$, the full real potential $\mathcal{V}_H(r;E)+\Delta\mathcal{V}(r;E)$, and the energy-independent potential $\mathcal{V}_H(r;E_F)$. The hatched areas indicate that the $1d_{\frac{5}{2}}$ and $1f_{\frac{5}{2}}$ single-particle strengths are spread; this spreading will be discussed in Sec. XII.

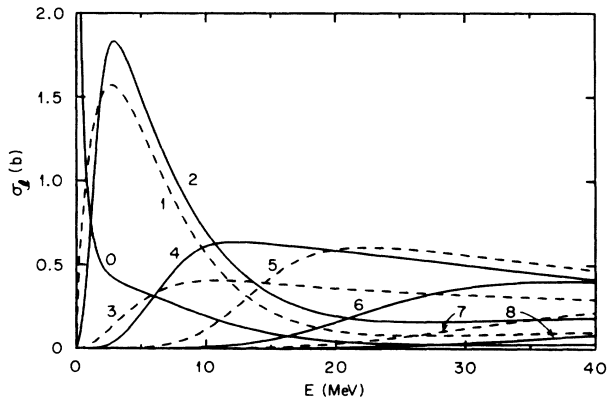

FIG. 11. Contribution to the total cross section of the partial waves with orbital angular momentum $l = 0$ to 8. The solid curves are associated with even and the dashed lines with odd values of l. Each curve represents the sum of the contributions associated with the total angular momenta $j = l + \frac{1}{2}$ and $j = l - \frac{1}{2}$.

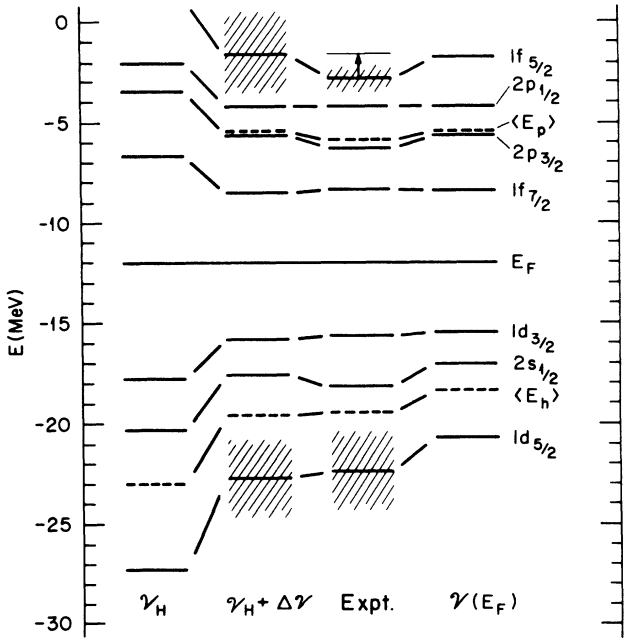

FIG. 12. Energies of the valence neutron single-particle states in ^{40}Ca. The column labeled Expt. contains experimental values taken from Ref. 26 in the case of particle states and from Ref. 27 in the case of hole states. The diagrams labeled $\mathcal{V}_H$ and $\mathcal{V}_H + \Delta\mathcal{V}$ give the energies calculated from the Hartree-Fock potential and from the real part of the full mean field, respectively. The column labeled $\mathcal{V}(E_F)$ contains the energies computed from the energy-independent potential $\mathcal{V}_H(r;E_F)$. The dashed horizontal lines represent the centroid energies of the particle and hole shells, Eqs. (9.1a) and (9.1b). The hatchings in the central two diagrams represent the domains over which the $1d_{\frac{5}{2}}$ and $1f_{\frac{5}{2}}$ single-particle strengths are spread (Sec. XII); in the case of the $1f_{\frac{5}{2}}$ strength in the Expt. column, the hatching has been terminated at -1.6 MeV to indicate the upper boundary of the experimental measurements (Ref. 26). The spin-orbit coupling is given by Eqs. (3.1a) and (3.1b).

The location of a shell is conveniently characterized by its centroid energy, namely

$$\langle E_p \rangle = \sum_{\text{uno}} (2j+1) E_{nlj} / \sum_{\text{uno}} (2j+1) , \tag{9.1a}$$

$$\langle E_h \rangle = \sum_{\text{occ}} (2j+1) E_{nlj} / \sum_{\text{occ}} (2j+1) , \tag{9.1b}$$

where uno and occ respectively refer to the subshells of the normally unoccupied ($E_{nlj} > E_F$) and occupied ($E_{nlj} < E_F$) valence shells. These centroid energies are represented by dashed horizontal lines in Fig. 12. The particle-hole gap is measured by the difference

$$\delta = \langle E_p \rangle - \langle E_h \rangle . \tag{9.2}$$

In the Hartree-Fock approximation the particle-hole gap is too large; within a given shell, the subshell energies are furthermore spread out too much relative to the experimental spectrum. As a matter of fact no $1f\frac{5}{2}$ level is bound in the Hartree-Fock approximation for which $\langle E_p \rangle$ is thus ill defined and is not shown in the left-hand column of Fig. 12. In contrast, the valence single-particle energies calculated from the full potential are in quite good agreement with the measured spectrum. We insist that this is achieved without adjusting any parameter. In our construction of the mean field the sole step at which a negative energy appeared was when we chose $V_H(E_F)$ in such a way that in the Hartree-Fock approximation the energies $E_{1f7/2}$ and $E_{1d3/2}$ are approximately symmetric about the experimental Fermi energy $E_F = -12$ MeV.

Near the Fermi energy, the addition of $\Delta\mathcal{V}(r;E)$ to $\mathcal{V}_H(r;E)$ has the following two main effects. (i) It decreases the energy dependence of the depth of the potential, see Fig. 4(b). (ii) It increases the potential radius for particle states ($E_{nlj} > E_F$) and decreases it for hole states ($E_{nlj} < E_F$), see Fig. 9. Both effects contribute to make the full potential more attractive than the Hartree-Fock contribution for particle states and less attractive for hole states. The two effects thus both tend to decrease the particle-hole energy gap. The quantitative nature of the agreement between the calculated and the measured single-particle spectrum indicates that the predicted dispersive contribution has a realistic radial and energy dependence.

The two columns on the right-hand side of Fig. 12 show that a passable agreement exists between the experimental valence single-particle spectrum and that calculated from the static potential $\mathcal{V}_H(r;E_F)$. Here, the word "static" refers to the fact that the potential depth and shape are independent of energy, as is the case for potentials used in many spectroscopic calculations. We note, however, that the agreement between the two columns on the right-hand side of Fig. 12 is fortuitous. Indeed, the compression of the spectrum of $\mathcal{V}_H(r;E_F)$ relative to that of $\mathcal{V}_H(r;E)$ is entirely due to the suppression of the energy dependence of the Hartree-Fock potential depth. In reality, most of the compression of the Hartree-Fock spectrum arises from the energy dependence of the potential radius near the Fermi energy. Consequently, one should not expect a static potential to correctly reproduce the radial shape of valence single-particle orbits.

X. DEEPLY BOUND SINGLE-PARTICLE STATES

In the present section we extrapolate the dispersive mean field down to large negative energies ($-80 < E < -20$ MeV) where deeply bound $1s$ and $1p$ single-particle orbits are expected. At these large negative energies the exponential parametrization (2.6) of $V_H(E)$ becomes unreliable; we discuss what type of energy dependence emerges from the fact that the energy dependence of our Hartree-Fock potential $\mathcal{V}_H(r;E)$ originates from the nonlocality of the microscopic Hartree-Fock mean field.

Little experimental information is available on the deeply bound neutron single-particle states in ^{40}Ca. In the ^{40}Ca$(p,pn)^{39}$Ca neutron knockout reaction a long tail in the neutron spectrum has been observed from -43 to about -30 MeV and has been ascribed to the $1p$ shell.[28] No peak appears in this broad distribution of $1p$ strength. We argue below that this should be ascribed to the fact that the peak is located near the lower end of the experimental range.

In the valence shells of ^{40}Ca the neutron and proton single energies are shifted with respect to one another by the same amount, which can be identified with the average Coulomb energy. More generally, the excitation energies are practically equal in ^{39}Ca as in ^{39}K. Therefore, it is quite reasonable to assume that the distributions of the $1p$ and $1s$ strengths are approximately the same in ^{39}Ca as in ^{39}K. In the latter case these strengths have been extracted from analyses of the ^{40}Ca$(p,2p)$ and ^{40}Ca$(e,e'p)$ reactions; a survey is given in Table X of Ref. 29. Here we adopt the proton separation energies obtained by Nakamura *et al.*[30] from the ^{40}Ca$(e,e'p)$ reaction. We combine them with the difference between the proton and neutron separation energies in ^{40}Ca to obtain the following estimates for the energies of the $1p$ and $1s$ neutron shells in ^{40}Ca, i.e., for the energies at which the corresponding distributions of single-particle strengths are expected to be maximum:

$$E_{1p} = -42.3 \text{ MeV}, \quad E_{1s} = -66.3 \text{ MeV} . \tag{10.1}$$

The uncertainties on these numbers may be as large as 5 to 10 MeV.[29] It should also be kept in mind that the $1s$ and $1p$ single-particle strengths are spread over a wide energy domain. This spreading will be discussed in Sec. XII.

We now compare the observed energies (10.1) with the predictions of our model. The $1p\frac{3}{2}$ and $1p\frac{1}{2}$ levels in our extrapolated potential $\mathcal{V}(r;E)$ lie at -49.8 and -43.2 MeV, respectively. Their centroid is thus equal to $\langle E_{1p} \rangle = -47.6$ MeV. The fact that this predicted binding is larger than the empirical one suggests that the extrapolated potential is too attractive at large negative energies. This is quite apparent for the deeper $1s$ single-particle state, whose predicted energy turns out to be about -250 MeV. This very large overbinding is related to the fact that the exponential parametrization of Eqs. (2.6) and (4.13) leads to an exponential divergence of the Hartree-Fock depth $V_H(E)$ when E tends towards minus infinity. The exponential parametrization (2.6) is thus unrealistic at large negative energies. Below we argue that a

linear energy dependence is more appropriate for energies smaller than the Fermi energy.

We first use the following approach to search a more realistic extrapolation of the Hartree-Fock depth towards large negative energies. We retain the same dispersive correction $\Delta\mathcal{V}(r;E)$ and the same radial shape for the Hartree-Fock potential as in the previous sections. We then adjust the depth of the Hartree-Fock potential in such a way that the full potential $\mathcal{V}(r;E_{nlj})$ has a bound state at the experimental single-particle energy E_{nlj}. We turn off the spin-orbit coupling in the case of the $1p$ shell since the experimental results combine the $1p_{\frac{3}{2}}$ and $1p_{\frac{1}{2}}$ single-particle strengths. Our results are represented by the solid dots in Fig. 13. In the case of the $1s$ and $1p$ shells, the calculated Hartree-Fock depths are equal to -88.8 and -75.5 MeV, respectively. They lie below the long-dashed curve which represents the exponential parametrization of Eqs. (2.6) and (4.13). As a matter of fact, they are extremely close to the linear extrapolation

$$V_H(E)=-58.8+0.55(E-E_F) \tag{10.2}$$

which is represented by the short-dashed curve in Fig. 13. Note that at the Fermi energy the linear function (10.2) has the same value and slope as the exponential parametrization, (2.6) and (4.13).

From a phenomenological point of view, it therefore appears preferable to approximate the energy dependence of the Hartree-Fock depth by a linear function in the domain $E<E_F$ and by an exponential function in the domain $E>E_F$. The difference between these two parametrizations is negligible in the domain of the valence single-particle energies, namely $|E-E_F|\lesssim 10$ Mev. We now show that these phenomenological features are in keeping with the fact that the energy dependence of our local Hartree-Fock potential actually derives from the nonlocality of the original microscopic Hartree-Fock mean field.

In the dispersive optical model, the Hartree-Fock mean field is a nonlocal energy-independent operator.[31] Nuclear-matter calculations indicate that in a uniform medium the nonlocality form factor approximately has a Gaussian shape, see, e.g., Fig. 32 of Ref. 32:

$$\mathcal{V}_{\rm PB}(\mathbf{r},\mathbf{r}')=\mathcal{V}_0\pi^{-3/2}\beta^{-3}\exp(-|\mathbf{r}-\mathbf{r}'|^2/\beta^2)\ ; \tag{10.3}$$

β is the range of nonlocality. The index PB refers to the fact that, in nuclei, this type of nonlocality has been considered by Perey and Buck.[2] One can use the following procedure for constructing a local energy-dependent potential which it approximately equivalent to the nonlocal operator (10.3) in the sense that it approximately predicts the same scattering phase shifts[2] and bound single-particle energies.[33] We henceforth only consider the nuclear center ($r=0$). The Fourier transform of the function (10.3) over the nonlocality variable $|\mathbf{r}-\mathbf{r}'|$ is given by

$$\mathcal{V}_{\rm PB}(k^2)=\mathcal{V}_0\exp(-\tfrac{1}{4}\beta^2k^2)\ . \tag{10.4}$$

The quantity $\hbar k$ can be identified with the nucleon momentum at the nuclear center. In the local momentum approximation it is related to the nucleon energy E by the following energy-momentum relation:

$$E=\hbar^2k^2/2m+\mathcal{V}_{\rm PB}(k^2)\ . \tag{10.5}$$

This defines a function $k(E)$. The quantity

$$V_{\rm PB}(E)=\mathcal{V}_{\rm PB}[k^2(E)]=\mathcal{V}_0\exp\left[-\frac{m\beta^2}{2\hbar^2}[E-V_{\rm PB}(E)]\right] \tag{10.6}$$

is the depth of the energy-dependent local potential which is approximately equivalent to the nonlocal operator (10.3).

The quantity $V_{\rm PB}(E)$ involves two parameters, namely a strength V_0 and a nonlocality range β. Here we take

$$\mathcal{V}_0=-130\ \text{MeV},\quad \beta=1.19\ \text{fm}\ . \tag{10.7a}$$

These values are chosen in such a way that $V_{\rm PB}(E)$ is close to the exponential parametrization of Eqs. (2.6) and (4.13) in the energy domain $E_F<E<40$ MeV. Equations (10.6) and (10.7a) yield

$$V_{\rm PB}(E_F)=-58.8\ \text{MeV}\ ,\qquad \left[\frac{d}{dE}V_{\rm PB}(E)\right]_{E=E_F}=0.50\ , \tag{10.7b}$$

which should be compared with Eqs. (4.13). The corresponding Perey-Buck-type depth is represented by the

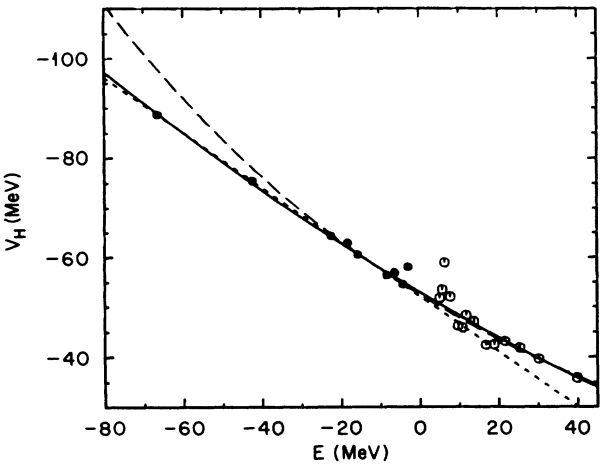

FIG. 13. Energy dependence of the depth of the Hartree-Fock potential. The open symbols are the same as in Fig. 4(b). The solid dots are located at the experimental single-particle energies; they represent Hartree-Fock depths adjusted in such a way that the full potential has a bound state at the observed single-particle energy, retaining the same dispersive correction as in Secs. IV and V (the spin-orbit coupling has been turned off in the case of the $1p$ shell). The long-dashed curve is the same as in Fig. 4(b): It represents the exponential parametrization of Eqs. (2.6), (2.9), and (4.13). The short-dashed straight line has the same value and slope as the long-dashed curve at the Fermi energy $E_F=-12$ MeV. The solid curve represents the depth of a local potential equivalent to a nonlocal field with a Perey-Buck-type nonlocality specified by Eqs. (10.6), (10.7a), and (10.7b).

solid curve in Fig. 13. It is practically equal to the linear parametrization of Eq. (10.2) for $E < E_F$ and to the exponential parametrization of Eqs. (2.6) and (4.13) for $E > E_F$. It very closely follows the empirical solid and open symbols. We note that the nonlocality range obtained here is similar to the value (0.85 fm) adopted by Perey and Buck in their original study.[2]

In conclusion, our previous phenomenological findings for the energy dependence of the depth of the Hartree-Fock potential are in agreement with the nonlocality of the original microscopic Hartree-Fock mean field. The Perey-Buck type of nonlocality provides a realistic description of this energy dependence.

XI. EFFECTIVE MASSES, OCCUPANCIES, AND SPECTROSCOPIC FACTORS

A. Effective masses

The effective mass $m^*(r;E)$ is defined as follows:

$$m^*(r;E)/m = 1 - \frac{d}{dE}\mathcal{V}(r;E) . \tag{11.1}$$

It describes the energy dependence of the real part of the mean field. In the Hartree-Fock approximation it becomes equal to

$$m_H^*(r;E)/m = 1 - \frac{d}{dE}\mathcal{V}_H(r;E) . \tag{11.2}$$

The difference between m^* and m_H^* is due to the energy dependence of the dispersive correction, which is characterized by the E mass $\overline{m}$:

$$\overline{m}(r;E)/m = 1 - \frac{d}{dE}\Delta\mathcal{V}(r;E) . \tag{11.3}$$

The long-dashed curve in Fig. 14 represents the Hartree-Fock effective mass at the Fermi energy. Note that the quantity $[1 - m_H^*(r;E)/m]$ has a Woods-Saxon shape at all energies since [Eq. (2.4)]

$$1 - m_H^*(r;E)/m = f(X_H)\frac{d}{dE}V_H(E) . \tag{11.4}$$

At the Fermi energy and at the nuclear center the parameter α of Eq. (4.13) yields

$$m_H^*(0;E_F)/m = 0.45 . \tag{11.5}$$

This is close to the effective mass associated with the Skyrme-IV effective nucleon-nucleon interaction (0.47, see Ref. 34) but is sizeably smaller than the effective mass of the Skyrme-M interaction (0.79, see Ref. 35). The latter is usually considered as more realistic because it yields better agreement with a number of empirical nuclear properties. One must, however, keep in mind that the Hartree-Fock potential determined in the present work should not be expected to yield good agreement with most of these properties. Indeed, it has to be supplemented by dispersive corrections. In contrast, usual Hartree-Fock fields are derived from phenomenological nucleon-nucleon interactions whose parameters are adjusted to yield good agreement with several nuclear properties in the Hartree-Fock approximation, i.e., without taking into account dispersive corrections (or equivalently without taking into account higher-order corrections in an expansion in powers of the strength of the effective nucleon-nucleon interaction).

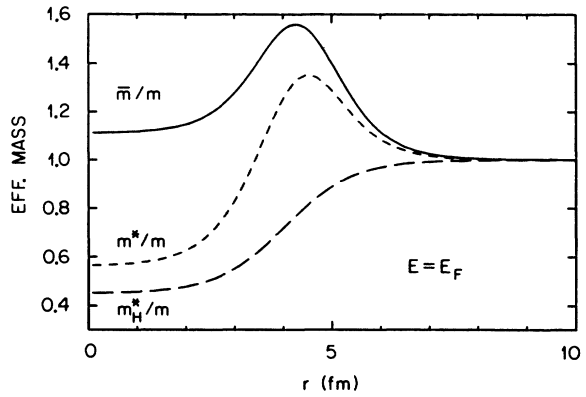

FIG. 14. Radial dependence of the quantities $m^*(r;E_F)/m$ (short-dashed line), $m_H^*(r;E_F)/m$ (long-dashed curve) and $\overline{m}(r;E_F)/m$ (solid curve).

The solid curve in Fig. 14 represents the radial dependence of the E mass at the Fermi energy. It presents a peak at the nuclear surface. This peak corresponds to the fact that the energy dependence of $\Delta\mathcal{V}_s(r;E)$ is particularly large for $r \approx R_s$ and E close to E_F [Fig. 5(b)]. It reflects the coupling of the single-particle state to the low-lying surface excitations of the ^{40}Ca core.

The short-dashed curve in Fig. 14 gives the radial dependence of the full effective mass at the Fermi energy. At the nuclear center one has

$$m^*(0;E_F)/m = 0.56 . \tag{11.6}$$

The difference between this value and its Hartree-Fock approximation [0.45, Eq. (11.5)] reminds one that the latter should be supplemented by dispersive corrections before being compared with empirical quantities. Moreover, the radial shape of $m^*(r;E_F)$ presents a peak near the nuclear surface, in contrast to the effective mass associated with phenomenological mean-field approximations. The peaking of $m^*(r;E_F)$ for $r \approx R_s$ sizeably enhances the calculated value of the nuclear density parameter and brings it in good agreement with the empirical value.[36]

B. Single-particle wave functions

We call $u_{nlj}(r) = u_{nlj}(r;E_{nlj})$ the radial part of the normalized bound eigenstates of $\mathcal{V}(r;E)$. In order to approximately take into account the fact that the original microscopic mean field is nonlocal, one should multiply these wave functions by the "Perey damping factor,"[2,37] namely by

$$P(r;E_{nlj}) = [m_H^*(r;E_{nlj})/m]^{1/2} . \tag{11.7a}$$

In the remainder of the present section we use the linear approximation (10.2), which is quite accurate for negative energies. The Perey damping factor is then independent

TABLE I. Calculated energy, root-mean-square radius, occupation probability, and spectroscopic strength of the neutron single-particle orbits in ^{40}Ca.

nlj	E_{nlj} (MeV)	$R_{nlj}^{\rm rms}$ (fm)	N_{nlj}	$\mathcal{S}_{nlj}$
$1f_{\frac{5}{2}}$	−1.50	4.69	0.07	0.92
$2p_{\frac{1}{2}}$	−4.19	5.08	0.07	0.89
$2p_{\frac{3}{2}}$	−5.59	4.81	0.08	0.85
$1f_{\frac{7}{2}}$	−8.54	4.04	0.12	0.75
$1d_{\frac{3}{2}}$	−15.79	3.51	0.89	0.78
$2s_{\frac{1}{2}}$	−17.53	3.64	0.91	0.81
$1d_{\frac{5}{2}}$	−22.48	3.38	0.93	0.90
$1p_{\frac{1}{2}}$	−39.12	2.81	0.96	0.97
$1p_{\frac{3}{2}}$	−43.8	2.84	0.96	0.97
$1s_{\frac{1}{2}}$	−66.12	2.24	0.97	0.96

of energy:

$$P(r)=[1-0.55f(X_H)]^{1/2} . \tag{11.7b}$$

We shall thus use the following function:[1]

$$\bar{u}_{nlj}(r)=C_{nlj}P(r)u_{nlj}(r) , \tag{11.8}$$

where the factor C_{nlj} is introduced for normalizing $\bar{u}_{nlj}(r)$. This quantity $\bar{u}_{nlj}(r)$ is the radial part of the overlap orbitals which play a major role in the analysis of one-nucleon transfer reactions.[38,39] The calculated root-mean-square radii

$$R_{nlj}^{\rm rms}=\left[\int_0^\infty \bar{u}^{\,2}_{nlj}(r)r^2dr\right]^{1/2} \tag{11.9}$$

of these single-particle orbits are given in Table I. It will be of interest to compare our prediction for the root-mean-square radius of the $1f_{\frac{7}{2}}$ orbit with the experimental value obtained from the analysis of the magnetic form factor $M7$ of ^{41}Ca which has just been measured.[40]

C. Occupation probabilities

Because of the residual nucleon-nucleon interaction the single-particle orbits which lie in the Fermi sea are not fully occupied and those which lie above the Fermi sea are not entirely empty. The occupation probability N_{nlj} can be estimated from the dispersive mean field.[41] In the case of a hole state ($E_{nlj}<E_F$) it is approximately equal to

$$N_{nlj}=\int_0^\infty \bar{u}^{\,2}_{nlj}(r)\times\left[1+\pi^{-1}\int_{E_F}^\infty \frac{\mathcal{W}(r;E')}{(E'-E_{nlj})^2}dE'\right]dr , \tag{11.10a}$$

while in the case of a particle state ($E_{nlj}>E_F$) one has

$$N_{nlj}=-\int_0^\infty \bar{u}^{\,2}_{nlj}(r)\times\left[\pi^{-1}\int_{-\infty}^{E_F} \frac{\mathcal{W}(r;E')}{(E'-E_{nlj})^2}dE'\right]dr . \tag{11.10b}$$

The calculated occupation probabilities are listed in Table I. These quantities are rather sensitive to the behavior assumed for $\mathcal{W}(r;E)$ at large $|E|$. They are also quite difficult to measure experimentally. In the case of protons, they can in principle be obtained by integrating the single-particle strength extracted from $(e,e'p)$ reactions. The uncertainty of the extracted values is very large. Indeed, the occupation probability obtained by the Tokyo group[30] for the proton shells in ^{40}Ca are 1.85 ($1s_{\frac{1}{2}}$), 1.7 (combined $1p_{\frac{1}{2}}$ and $1p_{\frac{3}{2}}$), 0.78 ($1d_{\frac{5}{2}}$), 1.05 ($1d_{\frac{3}{2}}$), and 1.0 ($2s_{\frac{1}{2}}$). Note that most of these numbers are larger than unity, which exhibits their unreliability. The measurements and analyses of the Saclay group[42] yield the following results, as quoted in Ref. 29: 0.75 ($1s_{\frac{1}{2}}$), 0.95 (combined $1p_{\frac{1}{2}}$ and $1p_{\frac{3}{2}}$), 0.77 (combined $1d_{\frac{5}{2}}$ and $1d_{\frac{3}{2}}$), and 0.65 ($2s_{\frac{1}{2}}$). The disparity between the two sets of empirical values reflects the difficulty of these analyses. In particular, the results are strongly affected by the tails of the distributions of the single-particle strengths, where severe background problems are encountered.

D. Spectroscopic factors

The strength of a quasiparticle excitation is given by the following expression:[41]

$$\mathcal{S}_{nlj}=\int_0^\infty \bar{u}^{\,2}_{nlj}(r)[m/\bar{m}(r;E_{nlj})]dr , \tag{11.11}$$

where $\bar{m}(r;E)$ is the E mass defined by Eqs. (11.3). The calculated $\mathcal{S}_{nlj}$ are listed in Table I. The physical meaning of these quantities is as follows.[43]

When E_{nlj} is very close to the Fermi energy, most of the strength of the corresponding single-particle state is contained in one, sometimes a few levels of ^{39}Ca or ^{41}Ca. Then the quasiparticle strength $\mathcal{S}_{nlj}$ can be identified with the spectroscopic factor of that level, or with the sum of the spectroscopic factors of the few levels which carry a sizeable strength. The spectroscopic factors extracted from analyses of one-nucleon transfer reactions are very sensitive to the radial shape of the single-particle orbits. In the case of proton orbits, the radial shape can potentially be accurately determined from $(e,e'p)$ reactions. This opens the possibility of measuring "absolute" spectroscopic factors.[44]

When E_{nlj} lies farther than a few MeV away from the Fermi energy the single-particle strength is distributed over many levels in ^{39}Ca or ^{41}Ca. Then the quantity $\mathcal{S}_{nlj}$ should be interpreted as the strength contained within a Lorentzian fitted to the peak of the distribution of single-particle strength. This distribution is discussed in the next section.

XII. SPECTRAL FUNCTIONS

Before discussing the spreading of single-particle strength it is useful to consider the case of nuclear matter. Then, the single-particle states are plane waves which are fully characterized by their wave number k (we disregard spin for simplicity). A one-hole configuration $(k)^{-1}$ is obtained by destroying a nucleon with momen-

tum k from the ground state $|0\rangle$ and a one-particle configuration $(k)^{+1}$ by creating a nucleon with momentum k on top of the ground state:

$$|k^{-1}\rangle = a_k|0\rangle, \quad |k^{+1}\rangle = a_k^+|0\rangle \ . \tag{12.1}$$

In the limit of a free Fermi gas, these one-hole or one-particle states would be stationary, i.e., would be eigenstates of the Hamiltonian and would have a well-defined energy. Actually, residual nucleon-nucleon interactions exist, and $|k^{-1}\rangle$ or $|k^{+1}\rangle$ therefore do not have a well-defined energy. The probability density of finding that these systems have an excitation energy $|E-E_F|$ is measured by the "spectral function" $S(k;E)$. The latter is given by[43]

$$S(k;E) = -\pi^{-1}\frac{\mathcal{W}(k;E)}{[E-\hbar^2k^2/2m-\mathcal{V}(k;E)]^2+[\mathcal{W}(k;E)]^2}, \tag{12.2}$$

where $\mathcal{V}(k;E)+i\mathcal{W}(k;E)$ is the mass operator (or self-energy). This distribution of single-particle strength presents a peak near the following "quasiparticle energy"

$$E_k = \hbar^2k^2/2m + \mathcal{V}(k;E_k) \ . \tag{12.3}$$

This relation reduces to Eq. (10.5) in the Hartree-Fock approximation, in which case $\mathcal{V}(k;E)$ is independent of E and $\mathcal{W}(k;E)=0$. The following sum rule holds:

$$\int_{-\infty}^{E_F} S(k;E)dE = n(k) \ , \tag{12.4}$$

where $n(k)$ is the occupation probability of the single-particle state $|k\rangle$.

In a nucleus the single-particle states are specified by quantum numbers (n,l,j). Then, the spectral function can be approximated by the following expression:[29]

$$S_{nlj}(E) = -\pi^{-1}\frac{\mathcal{W}_{nlj}(E)}{(E-E_{nlj})^2+[\mathcal{W}_{nlj}(E)]^2} \ , \tag{12.5}$$

where E_{nlj} is the single-particle energy of Table I, while

$$\mathcal{W}_{nlj}(r) = \int_0^\infty \bar{u}^2_{nlj}(r)\frac{\mathcal{W}(r;E)}{m^*(r;E)/m}dr \tag{12.6}$$

is the expectation value of the imaginary part of the mean field and $m^*(r;E)$ is the effective mass defined by Eq. (11.1). The origin of Eq. (12.6) has been discussed in connection with Eq. (4.5) of Ref. 1.

The expression (12.5) rests on a number of approximations,[29] in particular on the assumption that the spectral function is diagonal in the single-particle basis $\{n,l,j\}$. It presents the drawback that it does not automatically fulfill the approximate sum rule

$$\int_{-\infty}^{E_F} S_{nlj}(E)dE = N_{nlj} \ , \tag{12.7}$$

where N_{nlj} is the occupation probability of the single-particle orbit (n,l,j). This could easily be cured by introducing a normalization constant on the right-hand side of Eq. (12.5). We do not introduce it here mainly because the difference of this normalization factor from unity is much smaller than the uncertainties that affect the normalization of the experimental distribution of single-particle strength, and also because the sum rule (12.7) is only an approximation.

The spectral function $S_{1d5/2}$ predicted by Eq. (12.5) is represented by the solid curve in Fig. 15. We now compare it with the available empirical information. Doll *et al.*[27] measured the ^{40}Ca$(d,t)^{39}$Ca pickup cross section. They analyzed these data in the framework of the distorted-wave Born approximation. In the domain located between 4.3 and 9.5 MeV in ^{39}Ca, 20 levels with excitation energy $\epsilon^{(q)}_{5/2}$ were fed by the transfer of a neutron with orbital angular momentum $l=2$. They were assumed to be $\frac{5}{2}^+$ levels. The corresponding spectroscopic factors $\mathcal{S}^{(q)}_{d5/2}$ are listed in Table II of Ref. 27. The centroid energy of the observed distribution of $(d\frac{5}{2})^{-1}$ neutron hole strength is given by

$$E_{1d5/2} = \sum_{q=1}^{22} S^{(q)}_{d5/2}E^{(q)}_{d5/2} \ ; \tag{12.8a}$$

here

$$E^{(q)}_{5/2} = E_{1d3/2} - \epsilon^{(q)}_{5/2} \tag{12.8b}$$

is the binding energy associated with the level q. This empirical centroid energy is represented by a horizontal segment in the column labeled Expt. in Fig. 12. It is equal to -22.4 MeV, which is practically equal to the energy of the maximum of the calculated spectral function (-22.5 MeV).

In order to compare the shapes of the theoretical and empirical distributions, we construct an empirical histogram by dividing the spectroscopic factor $S^{(q)}_{d5/2}$ by the energy increment between the midpoint energies relative to the levels right above and below the level q. For the limiting upper and lower energy levels we use an energy in-

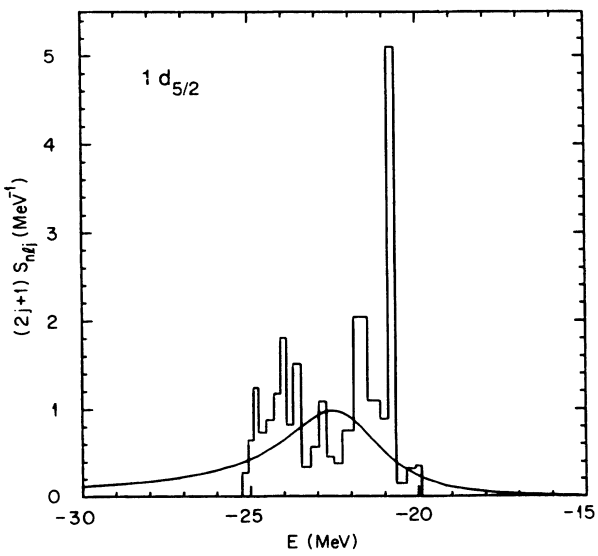

FIG. 15. Distribution of the $(2j+1)$-weighted neutron $d\frac{5}{2}$ single-particle strength in ^{40}Ca. The solid curve has been calculated from Eq. (12.5). The histogram has been constructed from the experimental data reported in Ref. 27, as described in the text.

crement equal to the last observed spacing. Figure 15 shows that the resulting histogram is in good agreement with the calculated spectral function. As we noted in Sec. XI, the measured spectroscopic factor should be ascribed a relative rather than an absolute meaning. To some extent this restriction also applies to the theoretical approximation (12.5). The following values are nevertheless of interest:

$$\int_{-30}^{E_F} S_{1d5/2}(E)dE = 0.95 \ , \qquad \int_{-26}^{-19} S_{1d5/2}(E)dE = 0.65 \ , \tag{12.9a}$$

where the integration limits are in units MeV. These numbers indicate that about 65% of the pickup strength should be expected to lie in the energy domain covered by the experimental data of Ref. 27, the rest being located at higher excitation energies. The centroid energy calculated over the experimental energy domain is found equal to

$$\int_{-26}^{-19} E S_{1d5/2}(E)dE \Big/ \int_{-26}^{-19} S_{1d5/2}(E)dE = -23.0 \text{ MeV} \ , \tag{12.9b}$$

which is close to the empirical value (−22.4 MeV).

We now turn to the distribution of the single-particle strength associated with the deeply bound $1p_{\frac{1}{2}}$, $1p_{\frac{3}{2}}$, and $1s_{\frac{1}{2}}$ orbits. The solid curve in Fig. 16 represents the quantity

$$S_h(E) = \sum_{n,l,j} (2j+1) S_{nlj}(E) \ , \tag{12.10}$$

where the sum extends over the $1d_{\frac{5}{2}}$, $1p_{\frac{1}{2}}$, $1p_{\frac{3}{2}}$, and $1s_{\frac{1}{2}}$ hole states. Each spectral function has been calculated from Eq. (12.5). The peaks of the calculated $1p$ and $1s$ spectral functions are located at −42 and −66 MeV, respectively. They practically coincide with the empirical estimates of Eqs. (10.1). More than half of the $1p$ strength lies deeper than −42 MeV. Therefore, it is rather natural that the ^{40}Ca$(p,pn)^{39}$Ca experiment of Ref. 28 did not exhibit a peak in the measured distribution, since the data only cover energies $E > -42$ MeV.

We now turn to the $1f_{\frac{5}{2}}$ orbit. The corresponding spectral function as predicted by Eq. (12.5) is represented by the solid curve in Fig. 17. We compare this prediction with the available empirical information. Belote *et al.*[26] measured the ^{40}Ca$(d,p)^{41}$Ca stripping cross section and analyzed it in the framework of the distorted-wave Born approximation. Their data extend up to 6.84 MeV excitation energy in ^{41}Ca, i.e., cover the binding-energy domain $-8.36 < E < -1.52$ MeV. Three of the observed levels were ascribed a significant $1f_{\frac{5}{2}}$ single-particle strength. The separation energies and quoted spectroscopic factors are, respectively, equal to −3.47 MeV ($S = 0.12$), −2.70 MeV ($S = 0.25$), and −2.55 MeV ($S = 0.11$). The corresponding centroid energy, evaluated as in Eq. (12.8a), is equal to −2.86 MeV. This value is represented by a horizontal segment in the column labeled Expt. in Fig. 12. It is more negative than the single-particle energy predicted by our dispersive mean field (see Table I and column $\mathcal{V}_H + \Delta\mathcal{V}$ in Fig. 12). However, this apparent discrepancy is deceptive. Indeed, the calculated spectral function indicates that the energy domain covered by the experimental data contains only a fraction (60%) of the single-particle strength of the calculated strength shown in Fig. 17 lies outside the domain $E < -1.5$ MeV. This is in keeping with the fact that the sum of the three spectroscopic factors quoted in Ref. 26 is equal to 0.47 (it reduces to 0.38 if one adopts the values cited in Ref. 45). We conclude that the energy of the $1f_{\frac{5}{2}}$ quasiparticle state is likely to be larger than the usually adopted value −2.86 MeV. Correspondingly, the agreement between the predicted and experimental single-particle energy of the $1f_{\frac{5}{2}}$ level is better than Figs. 5, 8, 12, and 13 suggest.

In summary, there exist a quite good agreement between the experimental and calculated distributions of

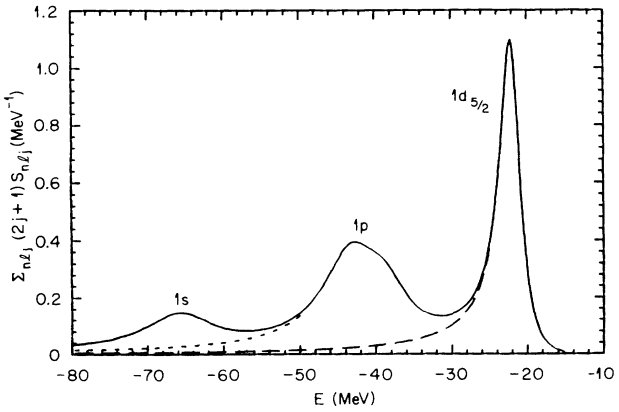

FIG. 16. The solid curve represents the weighted sum of the neutron-hole spectral functions, as defined by Eqs. (12.5) and (11.10). The long-dashed curve shows the contribution of the $1d_{\frac{5}{2}}$ spectral function, and the short-dashed line gives the tail of the sum of the $1d_{\frac{5}{2}}$, $1p_{\frac{3}{2}}$, and $1p_{\frac{1}{2}}$ contributions.

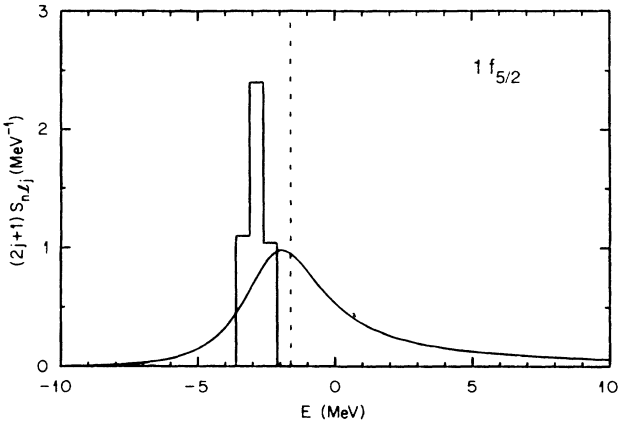

FIG. 17. Distribution of the $1f_{\frac{5}{2}}$ neutron single-particle strength. The solid curve has been calculated from Eq. (12.5). The histogram represents the empirical results reported in Refs. 26 and 45: They are normalized according to the spectroscopic factors of the three observed levels as quoted in Ref. 45. The dashed vertical line represents the upper end of the energy domain covered by the experimental data.

the single-particle strength. The expression (12.5) for the spectral function presents the interest that it vanishes for $E=E_F$. This property is not fulfilled by the usual quasiparticle approximation, in which the Green's function is approximated by the contribution of the quasiparticle pole [see e.g. (34.18) of Ref. 43]. The vanishing of $S_{nlj}(E)$ for $E=E_F$ gives rise to an asymmetry[46] of the quasiparticle peak whenever the difference $|E_{nlj}-E_F|$ is comparable to the spreading width, i.e., to

$$\Gamma^{\downarrow}_{nlj} \approx 2\mathcal{W}_{nlj}(E_{nlj}) \ . \tag{12.11}$$

This asymmetry is visible in Figs. 15 and 17. Caution must be exercised in the physical interpretation of $S_{nlj}(E)$, in particular when E approaches E_F, i.e., when the excitation energy in ^{39}Ca or ^{41}Ca approaches zero. Indeed, the concept of a density of single-particle strength has a meaning only when one can perform an average over levels. This is not possible for E close to E_F. For instance, no $\frac{5}{2}^+$ level has been identified below 4.3 MeV excitation energy in ^{39}Ca, i.e., for separation energies located between −20 and −15.64 MeV. In that energy domain the solid curve in Fig. 15 should not be ascribed any detailed physical meaning, except that its smallness reflects the property that little single-particle strength is expected to be located there. Note, moreover, that by using one average value for the Fermi energy [Eq. (2.9)] we have not taken into account the difference between the separation energy ($E_F^{(-)}=-15.64$ MeV) of ^{40}Ca and that ($E_F^{(+)}=-8.36$ MeV) of ^{41}Ca.[47] This is tolerable to the extent that $\mathcal{W}(r;E)$ is quite small between $E_F^{(+)}$ and $E_F^{(-)}$. These restrictions reflect the intrinsic limitation of the concept of a complex mean field to describe the nuclear dynamics. This mean field cannot aim at describing the full excitation spectrum of ^{39}Ca and ^{41}Ca. It can, however, describe average properties. For instance, we have seen in Sec. IX that it satisfactorily accounts, on the average, for the energy shift of that valence single-particle states close to the Fermi surface undergo because of their coupling to core excited states. It also yields estimates of the radial shapes of these valence orbits on their occupation probabilities and of their spectroscopic factors. Finally, we have shown in the present section that the dispersive mean field satisfactorily describes, on the average, the distribution of the single-particle strength of quasiparticle states which lie farther away from E_F.

XIII. REFINED MODEL AT LOW ENERGY

The solid curve in Fig. 3 shows that the total cross section predicted by our fixed-geometry model deviates from the experimental data for energies smaller than 9 MeV. This disagreement is not unexpected because the dispersive mean field only describes an average over many partial waves, while for $E<9$ MeV the total cross section is dominated by the partial waves associated with the orbital angular momenta $l=1$ and 2 (Fig. 11). The total cross section at small energy is thus sensitive to small changes in our model. This will be illustrated in the present section. We shall show that a good agreement between the calculated and experimental total cross sections is obtained if one introduces an energy dependence in the diffuseness a_s and radius parameter r_s that determine the radial shape of the surface-peaked absorption, Eqs. (3.5) and (3.6). This study is similar to the one that had been carried out in Sec. VI of Ref. 1 in the case of the n-^{208}Pb system. Other types of refinements could be proposed, for instance, one in which the absorption would depend upon angular momentum as was proposed in Sec. VII of Ref. 1 in the case n-^{208}Pb, see also Ref. 48. However, no convincing evidence for a systematic angular momentum dependence of the absorption would emerge in the present case since so few partial waves influence the n-^{40}Ca total cross section at low energy.

Since the type of refinement considered below is possibly not the most proper one, we will not search for an optimal parametrization of this "refined model." Accordingly, we retain the same volume components as in Sec. IV. We write the surface-peaked absorptive part of the potential as in Eqs. (3.5) and (3.6), but we now allow the corresponding shape parameters a_s, r_s to be energy dependent. However, we make the simplifying approximation that the corresponding real dispersive correction retains the same energy-independent radial shape as in the preceding sections (derivative of a Woods-Saxon with radius parameter 1.26 fm and diffuseness 0.60 fm).

In order to construct a parametrization adapted to this refined model, we perform least-squares fits of the experimental cross sections with the following four adjustable parameters: the shape parameters r_s, a_s of the surface-peaked absorption, the strength W_s of this surface ab-

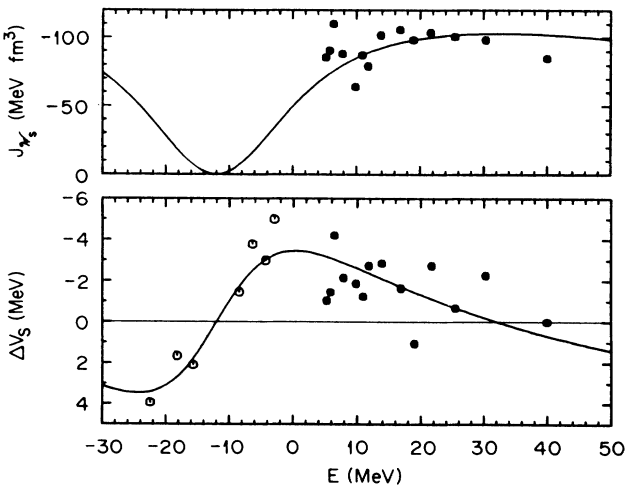

FIG. 18. The upper drawing represents the energy dependence of the volume integral per nucleon of the surface-peaked component of the imaginary part of the mean field; the lower drawing gives the strength of the real part of the surface-peaked component. The solid curves are derived from the solid curves in Fig. 5. The solid dots are obtained from four-parameter fits to the experimental cross sections, as described in Sec. XIII. The open symbols give the strength of surface component necessary for reproducing the experimental single-particle energies shown in the Expt. column of Fig. 12.

sorption, and the strength ΔV_s of the surface-peaked real potential. These fits are performed at each scattering energy independently. The solid dots in Fig. 18 represent the volume integral of the surface-peaked imaginary part and the strength of the surface-peaked real part obtained from these four-parameter fits to the experimental cross sections. The open symbols in the lower part of Fig. 18 are located at the experimental single-particle energies; they give the strength of the surface-peaked real potential that is needed to reproduce these energies. The solid curves are identical to those shown in Fig. 5 [after due multiplication by the geometric factor 14.9 fm^3 to derive the volume integral per nucleon associated with the solid curve in Fig. 5(a)]. Note that the curves in Fig. 18 are connected by a dispersion relation, since they are derived from Fig. 5. Figure 18 shows that the volume integrals obtained from the present four-parameter searches closely follow the volume integrals of the parametrization which had been adopted in Sec. V. We, therefore, retain the same parametrization of these volume integrals as in Sec. V. This fully determines the parametrization of the real strength $\Delta V_s(E)$ since the radial shape of the real surface-peaked component has been fixed.

In Fig. 19 the dots represent the least-squares adjusted values of r_s and a_s obtained from the four-parameter searches. Our "refined" model consists in taking into account the trend that below 10 MeV the diffuseness a_s of the surface-peaked imaginary part tends to be smaller than 0.60 fm while its radius parameter r_s tends to be larger than 1.26 fm. For illustration we adopt the following parametrization (lengths in fm, energies in MeV):

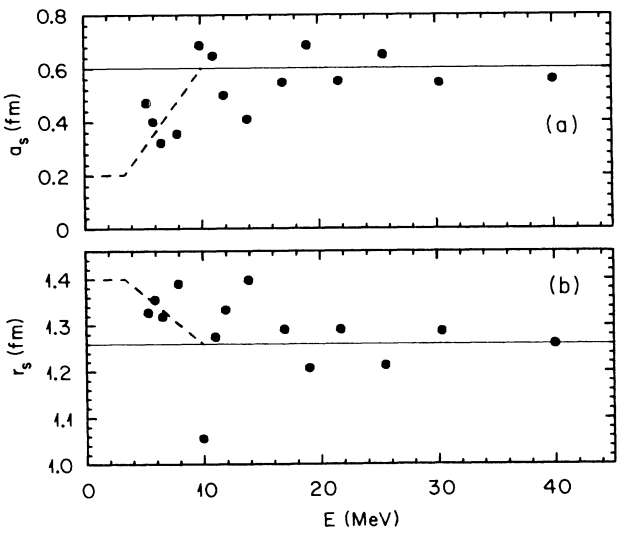

FIG. 19. Energy dependence of the diffuseness a_s and of the radius parameter r_s of the surface-peaked absorption for neutrons on ^{40}Ca. The solid dots are obtained from least-squares optical-model fits to the experimental cross sections with four adjustable parameters, namely a_s, r_s, W_s, and ΔV_s, as described in Sec. XIII. The horizontal solid lines show the energy-independent values adopted in Secs. IV–XII. The dashed segments represent the parametrization of Eqs. (13.1a)–(13.2c).

$$a_s = 0.20 \text{ fm} \quad \text{for } E_F < E < 3.35 , \tag{13.1a}$$

$$a_s = 0.20 + 0.060(E - 3.35) \quad \text{for } 3.35 < E < 10 , \tag{13.1b}$$

$$a_s = 0.60 \quad \text{for } 10 < E , \tag{13.1c}$$

$$r_s = 1.40 \quad \text{for } E_F < E < 3.35 , \tag{13.2a}$$

$$r_s = 1.40 - 0.021(E - 3.35) \quad \text{for } 3.35 < E < 10 , \tag{13.2b}$$

$$r_s = 1.26 \quad \text{for } 10 < E . \tag{13.2c}$$

This parametrization is represented by the dashed lines in Fig. 19, where the solid horizontals show the values adopted in our previous fixed-geometry model. The energy 3.55 MeV below which r_s and a_s are set constant has been somewhat arbitrarily chosen equal to the lowest neutron inelastic threshold, in analogy with the n-^{208}Pb case studied in Ref. 1. The energy 10 MeV above which r_s and a_s are constant is based on the observation that for $E > 10$ MeV, our fixed-geometry model yields good agreement with the experimental total cross section.

The total cross section predicted by the present refined model is represented by the dashed curve in Fig. 3. It is seen to be in close agreement with the experimental data. This fulfills our main purpose which was to illustrate that a slight modification of our fixed-geometry model is able to reproduce the measured total cross section at low energy. We note that the volume integrals per nucleon are exactly the same here as in the previous sections: The sole change is the radial shape of the surface-peaked component of the absorptive potential at low energy. The success of the present model should not be interpreted as an evidence that the type of refinement considered here is the correct one. In particular Fig. 19 shows that the specific parametrization of Eqs. (13.1a)–(13.2c) is rather arbitrary. Furthermore it must be kept in mind that another possible refinement would consist in introducing an angular momentum dependence in the fixed-geometry model, as was done in Sec. VII of Ref. 1 in the case of neutrons on ^{208}Pb, see also Ref. 48.

XIV. SUMMARY AND DISCUSSION

The dispersive optical-model analysis of the experimental cross sections consists in explicitly taking into account the dispersion relation which connects the real and imaginary parts of the mean field. This reduces the number of parameters which appear in the expression of the mean field. Moreover, this dispersive mean field automatically includes the complicated energy dependence of the real part that is associated with the fast decrease of the imaginary part as the nucleon energy approaches the Fermi energy. The latter property is quite important since the dispersive optical-model potential can then be extrapolated analytically from positive to negative energies. This extrapolation amounts to construct the shell-model potential from the optical-model potential. This is extremely useful since much more empirical information is available on the optical-model than on the shell-model potential.

In Ref. 1 a dispersive optical-model analysis had been carried out in the case of the n-^{208}Pb system. In the

present paper we perform it in the case of the n-^{40}Ca system. The main input of the calculation is the experimental differential, polarization, and total cross sections which are represented by the dots in Figs. 1–3. The solid curves in Figs. 1–3 are standard optical-model fits. Although the latter involve five or six parameters, adjusted at each energy independently, the quality of the fits is not very good. This partly reflects the limitation of the optical model in light-medium weight nuclei. *A fortiori*, one should not expect very good fits from the dispersive optical-model potential since it involves fewer parameters that, furthermore, are constrained to vary smoothly with energy.

As usual, the imaginary part of the mean field is written as a sum of volume and surface-peaked terms, Eq. (3.3). Except in Sec. XIII we use a fixed-geometry model in which it is assumed that the radial shapes of these two terms are independent of energy. Then the dispersion relation (2.3) predicts that the real part of the mean field also contains volume and surface-peaked dispersive corrections whose radial shapes are the same as those of the imaginary potential. These corrections vanish at the Fermi energy. They must be added to the Hartree-Fock potential which is assumed to have an energy-independent Woods-Saxon shape, with a depth that is an exponential function of energy. We argue in Sec. X that the latter assumption is quite realistic except for large negative energies where a linear energy dependence is more appropriate.

The central value of the real part of the full mean field is the sum of the depth of the Hartree-Fock potential and of that of the volume-dispersive contribution, since we assume throughout our analysis that the radial shape of the volume absorption is the same as that of the Hartree-Fock potential. The latter is determined by the dispersive relation. The energy dependence of the depth of the Hartree-Fock potential can then be obtained from the requirements that the empirical full depth be fitted and that the Fermi energy be reproduced. The depths of the full potential and of its Hartree-Fock component are represented in Fig. 4.

The strength of the surface-peaked dispersive contribution can be calculated from that of the surface-peaked absorption by means of the dispersive relation. It vanishes in the vicinity of 30 MeV (Fig. 5). There the radius parameter of the empirical full real potential is close to 1.18 fm. The latter value can then be identified with the radius parameters r_H of the Hartree-Fock potential, since this potential and the volume absorption have the same radius.

The value $r_H = 1.18$ fm obtained here for the n-^{40}Ca Hartree-Fock potential is smaller than that (1.24 fm) found for n-^{208}Pb in Ref. 1. It is argued in Sec. VII that this difference is in keeping with the property that the central densities of ^{40}Ca and ^{208}Pb are approximately the same. This allows one to derive the depth of the Hartree-Fock approximation to the symmetry potential by comparing the depths of the n-^{40}Ca and n-^{208}Pb Hartree-Fock potential. The result is represented in Fig. 10(a).

The dashed curves in Figs. 1 and 2 and the solid curve in Fig. 3 show that our fixed-geometry model is in fair agreement with the experimental cross sections, except for scattering energies smaller than 10 MeV. We emphasize that the expression "fixed geometry" refers to the radial shapes of the volume and surface-peaked imaginary potential and correspondingly of the dispersive contributions to the real part. Since the strengths of the dispersive contributions depend upon energy, the radial shape of the real part of the full mean field depends upon energy. In particular its radius decreases with increasing energy for $E > 10$ MeV (Fig. 9). A similar behavior was found for the n-^{208}Pb system,[1] in which case it had first been noticed on purely phenomenological grounds.[17,18]

The radius of the real part of the full mean field increases with energy in the negative energy domain (-20 MeV, 0), where the bound valence single-particle states are located. As a consequence the global attractive strength of the full real potential increases with energy in that domain, as illustrated by the volume integral per nucleon (Fig. 7). This is the main reason why the calculated bound-state energies are in good agreement with the experimental values, in contrast with the Hartree-Fock spectrum which has a too-large particle-hole energy gap as well as a too-large spacing between the subshells within the two valence shells (Fig. 12).

One of the intrinsic interests of ^{40}Ca is that the energies of the deeply bound $1p$ and $1s$ proton orbits have been localized. This yields a reliable estimate for the energies of the $1p$ and $1s$ neutron orbits. Our dispersive mean field strongly overbinds the $1s$ orbit (Sec. X). This is due to our assumption that the depth $U_{\rm HF}(E)$ of the Hartree-Fock potential is an exponential function of energy. The empirical energies are well reproduced if one adopts a linear energy dependence for $U_{\rm HF}(E)$ at negative energies. Thus, empirical evidence exists in favor of an exponential energy dependence of $U_{\rm HF}(E)$ at positive energy and of a linear dependence at negative energy. This can be understood from the fact that the energy dependence of the depth of our local Hartree-Fock potential actually reflects the nonlocality of the original microscopic Hartree-Fock field. A Perey-Buck type of nonlocality remarkably reproduces the energy dependence of $U_{\rm HF}(E)$ that had been deduced from our analysis (Fig. 13).

The dispersive mean field takes into account, in an average way, the effect of the residual nucleon-nucleon interaction. This is exhibited by the existence of an imaginary component in the mean field. As a consequence the dispersive mean field includes an average description of the deviations from the independent-particle model, in particular of the following facts. (i) The occupation probabilities of the single-particle orbits are smaller than unity inside the Fermi sea and different from zero outside the Fermi sea. (ii) The spectroscopic factors of the ground and excited single-particle levels of ^{39}Ca and ^{41}Ca are smaller than unity. Our analysis moreover predicts the radial shape of the single-particle orbits, in particular their root-mean-square radii. The calculated occupation probabilities, spectroscopic factors, and root-mean-square radii are listed in Table I.

When the excitation energy in ^{39}Ca or ^{41}Ca is larger than several MeV, there no longer exists one single level

that carries most of the single-particle strength. Rather, the single-particle strength is distributed over many levels. The average behavior of this distribution is described by the spectral function. It approximately has a Lorentzian shape. The location of its maximum can be identified with the single-particle (or quasiparticle) energy and its full width at half maximum with the single-particle spreading width. In the case of the $d\frac{5}{2}$ orbit our predicted spectral function is in good agreement with the measured distribution of the $l=2$ single-particle strength in ^{39}Ca (Fig. 15). Our predicted spectral functions for the $1p$ (Fig. 16) and $1f\frac{5}{2}$ (Fig. 17) orbits show that the energy domains covered by the presently available experimental data only extend over about half of the distribution. In particular, the $1f\frac{5}{2}$ orbit is most probably less bound than would be indicated by a straightforward interpretation of the experimental data.

Figure 3 shows that our fixed-geometry model yields a too-large total cross section for scattering energies smaller than 10 MeV. This is not unexpected since the mean field only describes an average over partial waves, while the total cross section at low energy is dominated by very few partial waves (Fig. 11). Moreover, the total cross section at low energy is quite sensitive to small modifications of the radial shapes of absorptive potential; this is exhibited in Sec. XIII. There we show that by decreasing the diffuseness and increasing the radius of the surface absorption, while keeping its volume integral unchanged, one can obtain a good agreement between the calculated and experimental total cross sections at low energy.

In conclusion, a dispersive optical-model analysis has been successfully performed for the n-^{40}Ca system. In particular it has been shown that this approach enables one to reliably extrapolate the optical-model potential down to the large negative energies of the most deeply bound orbits.

ACKNOWLEDGMENTS

We thank Dr. R. Sartor and Dr. D. C. Larson for stimulating discussions; Dr. R. Sartor has kindly calculated the solid curve in Fig. 13. We are indebted to Dr. W. Tornow for providing us with listings of the differential and polarization experimental cross sections measured at various laboratories. One of us (C.M.) acknowledges the hospitality and support of the Oak Ridge National Laboratory and the Joint Institute for Heavy Ion Research during part of this work. Oak Ridge National Laboratory is operated by Martin Marietta Energy Systems, Inc. for the U.S. Department of Energy under Contract No. DE-AC05-840R21400.

[1]C. H. Johnson, D. J. Horen, and C. Mahaux, Phys. Rev. C **36**, 2252 (1987).
[2]F. G. Perey and B. Buck, Nucl. Phys. **32**, 353 (1962).
[3]C. Y. Fu, At. Data Nucl. Data Tables **17**, 127 (1976).
[4]C. Y. Fu, private communication.
[5]J. D. Reber and J. D. Brandenberger, Phys. Rev. **163**, 1077 (1967).
[6]W. Tornow, E. Woye, G. Mack, C. E. Floyd, K. Murphy, P. P. Guss, S. A. Wender, R. C. Byrd, R. L. Walter, T. B. Clegg, and H. Leeb, Nucl. Phys. **A385**, 373 (1982); private communication.
[7]G. M. Honoré, W. Tornow, C. R. Howell, R. S. Pedroni, R. C. Byrd, R. L. Walter, and J. P. Delaroche, Phys. Rev. C **33**, 1129 (1986).
[8]J. Rapaport, J. D. Carlson, D. Bainum, T. S. Cheema, and R. W. Finlay, Nucl. Phys. **A286**, 232 (1977).
[9]R. Alarcon, J. Rapaport, and R. W. Finlay, Nucl. Phys. **A462**, 413 (1987).
[10]R. P. DeVito, S. M. Austin, W. Sterrenburg, and U. E. P. Berg, Phys. Rev. Lett. **47**, 628 (1981).
[11]D. C. Larson, D. M. Hetrick, and J. A. Harvey, Bull. Am. Phys. Soc. **25**, 543 (1980); private communication.
[12]J. P. Delaroche, P. P. Guss, G. M. Honoré, C. R. Howell, R. L. Walter, D. C. Larson, D. M. Hetrick, and J. A. Harvey, in *Neutron-Nucleus Collisions—A Probe of Nuclear Structure (Burr Oak State Park, Ohio, 1984)*, AIP Conf. Proc. No. 124, edited by J. Rapaport, R. W. Finlay, S. M. Grimes, and F. S. Dietrich (AIP, New York, 1985), p. 310.
[13]C. E. Zanelli, F. P. Brady, J. L. Romero, E. M. Castaneda, and D. L. Johnson, Phys. Rev. C **33**, 66 (1986).
[14]G. E. Brown and M. Rho, Nucl. Phys. **A372**, 397 (1981).
[15]A. M. Kobos and R. S. Mackintosh, J. Phys. G **5**, 97 (1979).
[16]A. M. Kobos and R. S. Mackintosh, Ann. Phys. (N.Y.) **123**, 296 (1979).
[17]J. R. M. Annand, R. W. Finlay, and F. S. Dietrich, Nucl. Phys. **A443**, 249 (1985).
[18]R. W. Finlay, J. R. M. Annand, J. S. Petler, and F. S. Dietrich, Phys. Lett. **155B**, 313 (1985); **157B**, 475 (1985).
[19]J. W. Negele, Phys. Rev. C **1**, 1260 (1970).
[20]C. Mahaux and R. Sartor, Nucl. Phys. **A481**, 407 (1988).
[21]Y. Wang and J. Rapaport, Nucl. Phys. **A454**, 359 (1986).
[22]S. P. Kwan, S. T. Lam, G. C. Neilson, and H. S. Sherif, Phys. Rev. C **31**, 271 (1985).
[23]M. Jaminon and C. Mahaux, Phys. Rev. C **34**, 2084 (1986).
[24]G. M. Honoré, Ph.D. dissertation, Duke University, 1986 (University Microfilms, 300 N. Zeeb Rd., Ann. Arbor, MI 48106).
[25]J. P. Delaroche and W. Tornow, Phys. Lett. B **203**, 4 (1988).
[26]T. A. Belote, A. Sperduto, and W. W. Buechner, Phys. Rev. **139**, B80 (1965).
[27]P. Doll, G. J. Wagner, K. T. Knöpfle, and G. Mairle, Nucl. Phys. **A263**, 210 (1976).
[28]J. W. Watson, M. Ahmad, D. W. Devins, B. S. Flanders, D. L. Friesel, N. S. Chant, P. G. Roos, and J. Wastell, Phys. Rev. C **26**, 961 (1982).
[29]S. Frullani and J. Mougey, in *Advances in Nuclear Physics*, edited by J. W. Negele and E. Vogt (Plenum, New York, 1984), Vol. 14, p. 1.
[30]K. Nakamura, S. Hiramatsu, T. Kamae, H. Muramatsu, N. Izutsu, and Y. Watase, Nucl. Phys. **A271**, 221 (1976).
[31]C. Mahaux and R. Sartor, Nucl. Phys. **A468**, 193 (1987).
[32]J. P. Jeukenne, A. Lejeune, and C. Mahaux, Phys. Rep. **25C**, 83 (1976).
[33]W. Ulrici and W. R. Hering, Nucl. Phys. **A110**, 281 (1968).

[34]M. Beiner, H. Flocard, Nguyen Van Giai, and P. Quentin, Nucl. Phys. **A238**, 29 (1975).
[35]J. Bartel, P. Quentin, M. Brack, C. Guet, and H.-B. Håkansson, Nucl. Phys. **A386**, 79 (1979).
[36]C. Mahaux and R. Sartor, Nucl. Phys. **A475**, 247 (1987).
[37]F. G. Perey, in *Direct Interactions and Nuclear Reaction Mechanisms,* edited by E. Clementel and C. Villi (Gordon & Breach, New York, 1963), p. 125.
[38]M. Jaminon, C. Mahaux, and H. Ngô, in *Proceedings of the 1987 CEBAF Workshop,* edited by F. Gross and C. Williamson (CEBAF, Newport News, 1987), p. 238.
[39]G. R. Satchler, *Direct Nuclear Reactions* (Oxford University Press, New York, 1983).
[40]A. Aroum, P. Bricault, P. Dreux, J. Dupont, C. Goodman, D. Goutte, B. Frois, Y. Kroll, V. Méot, X. H. Phan, S. Platchkov, S. Raman, I. Sick, and P. de Witt Huberts, Annual Report No. CEA-N-2550, Saclay, France, 1987 (unpublished); Phys. Rev. Lett. (in press).
[41]C. Mahaux and H. Ngô, Nucl. Phys. **A431**, 486 (1984).
[42]J. Mougey, M. Bernheim, A. Bussière, A. Gillebert, Phan Xuan Hô, M. Priou, D. Royer, I. Sick, and G. J. Wagner, Nucl. Phys. **A262**, 461 (1976).
[43]C. Mahaux, P. F. Bortignon, R. A. Broglia, and C. H. Dasso, Phys. Rep. **120**, 1 (1985).
[44]A. E. L. Dieperink and I. Sick, Phys. Lett. **109B**, 1 (1982).
[45]P. M. Endt and C. Van der Leun, Nucl. Phys. **A214**, 1 (1973).
[46]H. Orland and R. Schaeffer, Nucl. Phys. **A299**, 442 (1978).
[47]J. P. Jeukenne and C. Mahaux, Nucl. Phys. **A394**, 445 (1983).
[48]C. H. Johnson and R. R. Winters, Phys. Rev. C **37**, 2340 (1988).